WIRELESS POWER TRANSFER FOR RAILWAY ELECTRIFICATION

by

Xiuhu Sun

A thesis submitted to the faculty of
The University of North Carolina at Charlotte
in partial fulfillment of the requirements
for the degree of Master of Science in
Electrical Engineering

Charlotte

2023

Approved by:

_____
Dr. Tiefu Zhao

_____
Dr. Michael Mazzola

_____
Dr. Shen-En Chen

ABSTRACT

XIUHU SUN. Wireless Power Transfer for Railway Electrification.
(Under the direction of DR. TIEFU ZHAO)

This thesis explores the innovative realm of wireless power transfer (WPT), with a specific focus on its application in railway electrification, an area not extensively addressed in the existing literature, particularly concerning dynamic motion analysis. The research introduces a 6 kW dynamic multiple-transmitter and single receiver WPT system tailored for railway vehicles, employing a parallel synchronous multiple LCL-S compensation topology.

Comprehensive static and dynamic tests were conducted to evaluate the system's performance. In static testing, the system demonstrated remarkable DC-to-DC efficiency, reaching up to 94.73% with an output of 3.0 kW. Dynamic testing further confirmed the system's robustness, showcasing stable output and sustained efficiency, indicative of its potential for seamless integration into railway systems.

Another aspect of the study involves electromagnetic field (EMF) testing to ensure the system's safety and compliance with established standards. The results from these tests provide crucial insights into the EMF emissions of the WPT system.

Furthermore, the thesis delves into various application scenarios, illustrating the versatility of the WPT system in different railway contexts. From retrofitting existing railway systems to integration in newly constructed networks, the study showcases the broad potential of WPT technology in transforming railway electrification.

ACKNOWLEDGEMENTS

I am deeply grateful for the invaluable support and guidance provided by my advisor, Dr. Tiefu Zhao, throughout the journey of my study. His expertise, patience, and encouragement have been instrumental in shaping the direction of my research and fostering my academic growth.

I sincerely thank Dr. Shen-En Chen, who has worked closely with Dr. Zhao, for providing detailed and thoughtful assistance for my studies and research in the past two years. Additionally, as a member of my thesis committee, Dr. Chen has offered valuable suggestions for the revision of my thesis.

I would also like to express my sincere gratitude to my committee member, Dr. Michael Mazzola, whose long-term support and guidance have been indispensable in advancing this project. His insightful suggestions have greatly inspired my future research endeavors as well.

I owe a debt of gratitude to my beloved family for their unwavering love and support. My dear wife, Dr. Mingxia Liu, and my precious daughter, Cathy Sun, whose understanding and encouragement have been a constant source of motivation and strength for me.

Furthermore, I wish to acknowledge the support of my colleagues and friends at UNC Charlotte for providing invaluable assistance and resources throughout the course of this research.

I am genuinely grateful to all of you for being an integral part of my academic journey and contributing to the success of this thesis.

DEDICATION

This thesis is dedicated to my cherished wife, Mingxia Liu. Her unwavering emotional support and generous financial assistance have been pivotal in my pursuit of aspirations. She is not only my most steadfast encourager but also the person I hold most dear.

TABLE OF CONTENTS

LIST OF TABLES

LIST OF FIGURES

LIST OF ABBREVIATIONS

A	Ampere, Amp
AC	Alternating Current
APT	Acoustic Power Transfer
AWG	American Wire Gauge
CO2	Carbon Dioxide
CPT	Capacitive Power Transfer
DC	Direct Current
DRL	Dosimetric Reference Limit
DSP	Digital Signal Processor
EM	Electromagnetic Meter
EMF	Electromagnetic Field
EMI	Electromagnetic Interference
ERL	Exposure Reference Level
ESR_{in}	Input Equivalent Series Resistance
EV	Electric Vehicle
FEA	Finite Element Analysis
GHG	Greenhouse Gas
HF	High-frequency
ICNIRP	International Commission on Non-Ionizing Radiation Protection
IEEE	Institute of Electrical and Electronics Engineers
IPT	Inductive Power Transfer
k	Coupling Factor

kW	Kilowatt
M	Mutual Inductance
MEF	Material Effect Factor
mmf	Magnetomotive Force
MOSFET	Metal-Oxide-Semiconductor Field-Effect Transistor
MPT	Microwave Power Transfer
Ms	Millisecond
MTSR	Multiple-Transmitter and Single-Receiver
nF	Nanofarad
OPT	Optical Power Transfer
PCB	Printed Circuit Board
RF	Radio Frequency
Rx	Receiver
S	Second
SiC	Silicon Carbide
SoC	State of charge
STSR	Single-Transmitter and Single-Receiver
T	Tesla
TCO	Total Cost of Ownership
Tx	Transmitter
V	Volt
VA	Volt-Amp
W	Watt

WPT	Wireless Power Transfer
Ω	Ohm
μH	Microhenry
μT	Microtesla

CHAPTER 1: INTRODUCTION

1.1 U.S. Railway

In the United States, railroads are predominantly utilized for transporting goods, like coal, grains, fertilizers, and various raw materials. The U.S. freight rail network is known for being the largest, safest, and most cost-efficient freight system globally. This extensive system stretches over 136,667 miles [1], and as of 2021, it boasted a fleet of 23,264 freight locomotives [2]. In contrast, passenger rail services occupy a smaller segment of the railway market. These services are primarily offered by the National Railroad Passenger Corporation, known as Amtrak, whose network covers 20,787 miles. In 2020, Amtrak operated 384 passenger locomotives [3].

Currently, the predominant types of railway locomotives are electric and diesel. Electric locomotives are favored over their diesel counterparts due to higher efficiency, lower operating costs, and reduced emissions. This preference has led to their widespread adoption globally, thereby hastening the process of railway electrification. Nevertheless, in the United States, the electrification rate is surprisingly low, at less than 1% [4]. This situation is attributed to a mix of historical, economic, and regulatory factors [5].

There are indeed arguments against transitioning to electric locomotives, primarily centered around the extensive reforms required in infrastructure, staff training, and operations [6]. Such a transition poses significant challenges and entails considerable costs. Electrifying only portions of the railway could lead to substantial expenses and efficiency losses when switching locomotives between electrified and non-electrified sections. Moreover, the process of railway electrification is complex and time-consuming, involving

intricate construction and approval procedures that could disrupt railway operations. For these reasons, the United States is characterized by a relatively low degree of railway electrification and slow progress in its electrification process.

1.2 Battery-Electric Locomotives vs. Diesel Locomotives

1.2.1 Introduction of Diesel and Battery-Electric Locomotives

Diesel locomotives are powered by diesel engines. These engines drive a generator or an alternator to produce electric or mechanical power that propels the train. In this thesis, the term also includes diesel-electric locomotives.

Battery-electric locomotives are powered by large batteries that store electric energy. With advancements in battery technology, this type of locomotive is increasingly becoming a viable and eco-friendly option. Compared to diesel locomotives, the main advantages of battery-electric locomotives are evident in environmental protection, higher efficiency, lower total cost of ownership (TCO), and energy diversity.

1.2.2 Environmental Protection

Battery-electric locomotives offer significant environmental benefits. These trains are powered by electricity, so they do not directly produce exhaust emissions. In comparison to trains relying on fossil fuels (such as diesel), electric trains can substantially reduce air pollution and greenhouse gas (GHG) emissions.

1.2.3 Efficiency

Battery-electric locomotives are highly efficient [7]. The conversion efficiency of electric locomotives (including energy conversion from the grid to the wheels and regenerative braking efficiency) can reach about 85%. The efficiency of the battery's charging and discharging process is 90% each. The overall efficiency of battery-electric

locomotives can reach 69%, while diesel locomotives have an efficiency of only 39%. The efficiency of battery-electric locomotives is significantly higher than that of diesel locomotives.

1.2.4 TCO

Diesel locomotives can be converted into battery-electric locomotives by adding battery tender cars [8]. Though battery trains initially require higher equipment and infrastructure investments, they surpass diesel trains in terms of maintenance, energy consumption, pollutant emissions, and GHG emissions.

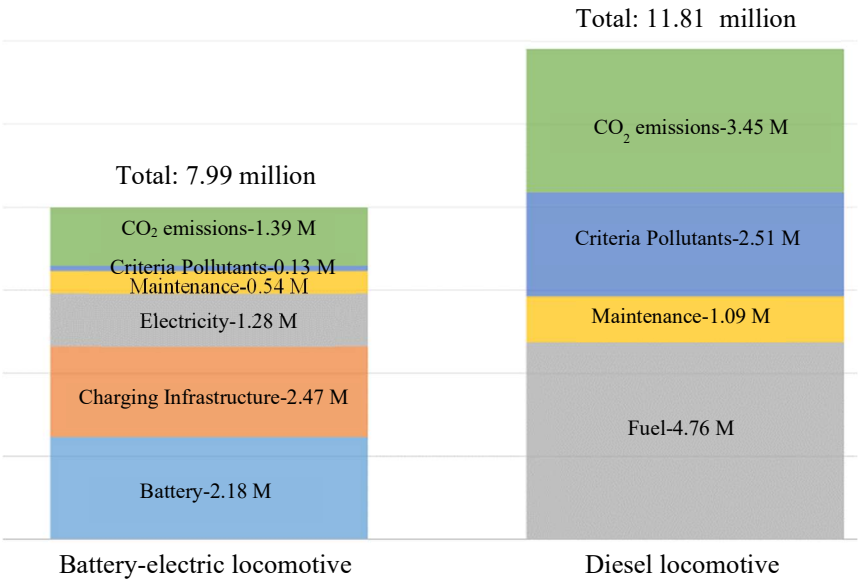

Figure 1-1: TCO of locomotives by over 20 years

Figure 1-1 illustrates the 20-year TCO for both battery-electric and diesel locomotives [8]. The modification cost of battery-electric locomotives is $4.65 million for battery and charging infrastructure, with a TCO of $7.99 million. In comparison, the TCO for diesel locomotives is $11.81 million. The TCO for battery trains is only 67.65% of that of diesel locomotives, which is 32.3% lower. The cost savings amount to $3.82 million, with a return on investment of 82.15%. In terms of energy consumption, maintenance,

pollutant, and CO2 emission costs, battery-electric locomotives are only 26.89%, 49.54%, 5.18%, and 40.29% of the costs of diesel locomotives, respectively. Thus, converting trains to battery-electric is economically viable.

1.2.5 Energy Flexibility

Electric locomotives draw energy from the grid, which can be generated from various sources, allowing them to utilize multiple energy types. As the proportion of renewable energy (such as wind, solar, and hydropower) in electricity production increases, the GHG emissions of electric trains will further decrease.

In contrast, diesel locomotives rely on burning diesel as their energy source, producing significant GHG emissions, including carbon dioxide, carbon monoxide, and nitrogen oxides. Although emissions can be somewhat reduced through improved engine design and the use of cleaner fuels, the GHG emissions from diesel trains have a hard limit.

1.2.6 Other Advantages

Electric locomotives typically produce less noise and vibration, thereby reducing their impact on communities and the environment along their routes. Additionally, they have more flexible start-stop capabilities, making them well-suited for high-frequency urban and suburban transport services that require dense scheduling.

1.3 WPT

1.3.1 Generalized WPT

Generalized defined wireless power transfer or wireless power transmission, classified by technical category, includes acoustic power transfer (APT), optical power transfer (OPT), microwave power transfer (MPT), inductive power transfer (IPT), and capacitive power transfer (CPT) [9].

In the field of electric power, the three common methods of WPT are CPT, MPT, and IPT. The CPT transmits electricity using electric fields between metal electrodes fields. The problems of CPT are short distances and restricted applications. The MPT converts electrical power at the transmitter side and typically consists of a power source, a microwave generator, and a transmitting antenna. The receiver side combines a rectifier and an antenna, which can capture the transmitted microwaves and convert them back into direct current (DC) electricity. MPT solves the problem of distance, but the efficiency is low and unsuitable for high-power energy transmission. The IPT refers to the transfer of electrical energy between a transmitting end and a receiving end by a resonant electromagnetic field without physical wired connections. It has the capability of transmitting high power at high efficiency. The problem is that the distance is short. Figure 1-2 illustrates three methods of wireless power transfer: (a) CPT, (b) MPT, and (c) IPT.

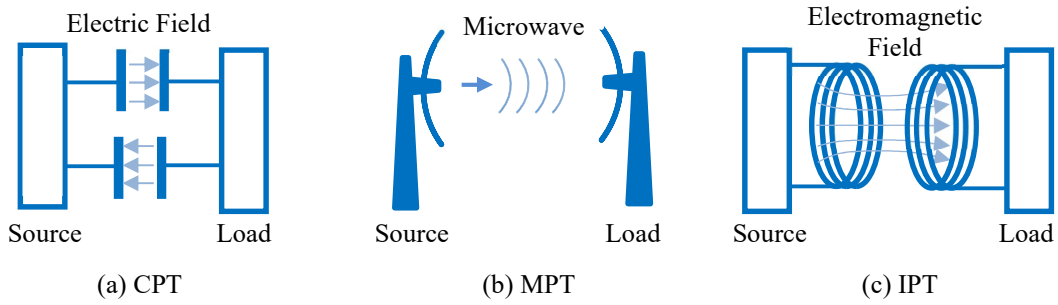

Figure 1-2: Three methods of wireless power transfer

1.3.2 IPT

This thesis focuses on IPT, which is often referred to as WPT.

WPT without a magnetic core was first proposed by Nikola Tesla to supply wireless mains power over long distances around 100 years ago [10]. This process can be unidirectional or bidirectional. The transmitting end is powered by a direct current source,

and the transmitting coils transfer energy to the receiving coils through variations in the electromagnetic field. Subsequently, the receiving coil supplies power to the load. Commonly, the process involves converting DC to high-frequency AC on the transmitting side, generating an electromagnetic field, and then converting the field back to high-frequency AC on the receiving side and back to DC. Compared to traditional methods of transmitting DC or AC directly through cables, WPT is more complex in structure, has higher costs and lower efficiency. However, WPT eliminates the need for wires and sockets, enhances the system's power transfer capability, and enables power transfer during movement (dynamic), offering unparalleled convenience compared to wired transmission. As a result, wireless power transmission has gained more profound research and wider applications in recent years.

1.4 Motivation

1.4.1 Research Questions

The United States has the world's largest railway network and the most trains, with less than 1% of it electrified. This starkly contrasts other countries worldwide actively promoting energy conservation and emissions reduction through the substantial development of electrified railways.

Reference [8] outlines a battery-driven locomotive retrofit approach equipped with 14 megawatt-hours of batteries and inverters, enabling a range of 241 kilometers while consuming only half the energy of diesel trains. This battery-driven locomotive retrofit approach accomplishes railway electrification while avoiding the substantial investments associated with track electrification, making it a potential option for future railway electrification in the United States.

An essential challenge for battery-electric trains is charging. Currently, available charging methods include charging of batteries over catenary [11, 12], battery tenders [13], plug-in [14], and wireless charging [14, 15]. Among them, wireless charging using IPT based on magnetic resonance coupling stands out for its electrical isolation, high power capabilities, and compatibility with other systems, making it a potential primary charging technology for battery-electric locomotives.

In addition, wireless power transfer offers several advantages over traditional railway power supply methods, such as overhead wires and third rails. First, wireless power transfer systems are typically more environmentally friendly as they do not require extensive copper wires and support structures, reducing resource consumption and minimizing disruption to the natural environment. Second, wireless power transfer systems usually do not necessitate large railway overhead wires or third rails, visually improving the aesthetics of railway routes. Third, wireless power transfer systems are also more flexible and can be moved or redeployed as needed to meet the requirements of different railway routes, while traditional power supply methods require more infrastructure modifications. Fourth, wireless power transfer systems can reduce energy losses during electricity transmission, enhancing energy utilization efficiency and reducing energy costs. Furthermore, wireless power transfer does not involve contact wires or high-voltage third rails, reducing safety risks in railway systems and decreasing the likelihood of accidents. Finally, wireless power transfer is the most feasible or even the only viable power supply method for future dominant railway transportation modes such as magnetic levitation (Maglev) and super-high-speed trains.

This thesis will focus on charging battery-electric locomotives using WPT

technology. It aims to support the electrification of the U.S. railway system and ultimately reduce pollution and GHG emissions in the railway sector.

1.4.2 Research Contents

In this thesis, the research contents include:

(1) A literature review on WPT for EVs and railways, which covers topics such as topologies, couplers, and WPT efficiencies.

(2) The design of a WPT topology for dynamic charging, including an analysis of characteristics, voltage calculations, and coupling factor calculations.

(3) The design and manufacturing of a WPT prototype, encompassing inverter and rectifier circuit boards as well as the mechanical structure.

(4) Testing the system, which involves static testing, dynamic testing, and electromagnetic field (EMF) testing.

(5) The introduction of future application scenarios, including the Belmont Trolley and new potential application scenarios.

1.5 Organization of the Thesis

This thesis is structured to comprehensively explore WPT technology in the context of railway applications, with a specific focus on WPT for charging the battery-electric locomotives. It is organized as follows:

Chapter 1: Introduction

This chapter sets the stage by introducing the U.S. railway system, the emergence of battery-electric locomotives, and the WPT technology within the railway landscape. It outlines the motivations behind this research, poses the research questions to be addressed, and provides an overview of the content covered in subsequent chapters.

Chapter 2: Literature Review

A literature review related to WPT is presented here, encompassing WPT applications in electric vehicles (EVs) and railways, and discussions on various topologies, coupler designs, and efficiencies.

Chapter 3: WPT Design for Locomotives

The third chapter delves into the core of the research, focusing on the design aspects of WPT systems tailored for locomotives, including discussing the system structure, introducing the LCL-S compensation topology, and presenting the innovative W-I-shaped coupler.

Chapter 4: Prototype Development

This chapter details the practical implementation of the research, describing the components involved in both the transmitter and receiver sides of the WPT system. Additionally, auxiliary equipment such as tracks and movable platform are outlined, culminating in an overview of the prototype development.

Chapter 5: Static and Dynamic Analysis

This chapter undertakes a comprehensive analysis of the WPT system's performance. It investigates static experiments, dynamic experiments and electromagnetic interference (EMI) analysis.

Chapter 6: Future Application

This chapter expands on the practical implications of the research by discussing potential application scenarios for WPT technology in railway systems. Case studies, such as the Belmont Trolley Project, are examined to showcase the feasibility and benefits of WPT implementation.

Chapter 7: Conclusion and Future Work

The final chapter summarizes the essential findings and contributions of the thesis. It also outlines potential avenues for future research and development in dynamic wireless power transfer for railway applications.

References and Appendix

References and Appendix are provided at the end of the thesis to offer sources and additional technical details related to the research.

CHAPTER 2: LITERATURE REVIEW

2.1 WPT for EV Applications

High-power wireless charging is currently the most researched in EVs. Compared to wired charging, wireless charging offers several advantages:

(1) Simplified charging process: Wireless charging eliminates the need to connect a charger to the vehicle. Simply parking the vehicle on a charging pad simplifies the charging process.

(2) Reduced wear and tear: Without the need for physical plugs and sockets, wireless charging reduces physical wear and tear, enhancing reliability.

(3) Versatility: Wireless charging is versatile, accommodating various vehicle models. This reduces the need for multiple types of chargers and saves resources.

(4) Incorporation into roads: Wireless charging can be embedded into roadways, enabling charging while driving. This approach saves charging time and lessens the necessity for large-capacity batteries in vehicles [16-18].

(5) Automated operation: Wireless charging can be fully automated, complementing and promoting the development of autonomous driving technology [19].

Given these benefits, and with the proliferation of EVs and increasing demand driven by the rapid development of autonomous driving technology, wireless charging demonstrates significant potential for widespread application in vehicle charging. Consequently, wireless charging for EVs has attracted extensive and in-depth research.

2.2 WPT for Railway Applications

Electrifying traditional railways is crucial to improve efficiency and make them

more environmentally friendly, yet the high cost presents a considerable challenge. An alternative approach involves retrofitting locomotives with batteries and chargers, which are then charged using cables when the vehicle is stationary. However, wired charging is often hindered by the complexity of the process and weather limitations. Moreover, heavy high-voltage cables pose labor-intensive work and risks of electric shock.

To address these challenges, WPT has been introduced for railway applications. By eliminating a portion of the cable between the power source and the locomotive, WPT can charge the vehicle during parking or even while in motion without human intervention. Consequently, WPT reduces parking charging time and allows for smaller battery packs, enhancing overall economy and usability.

2.3 Topologies

WPT systems transfer power from a source to a load through a non-galvanic connection, typically an air gap, between the coupling coils. This leads to large leakage inductance and small mutual inductance, resulting in high current and power loss, and thus low efficiency [20].

A capacitor compensates for the circuit to address this problem, reducing the losses caused by circulating current and thereby increasing efficiency. Compensation on the transmitter side decreases the VA rating, while on the receiver side, it enhances power transfer capability [21].

Figure 2-1 shows four basic topologies labeled as SS, SP, PP, and PS for inductive WPT systems. The first S or P indicates series or parallel compensation of the primary winding, and the second S or P indicates the same for the secondary winding [22].

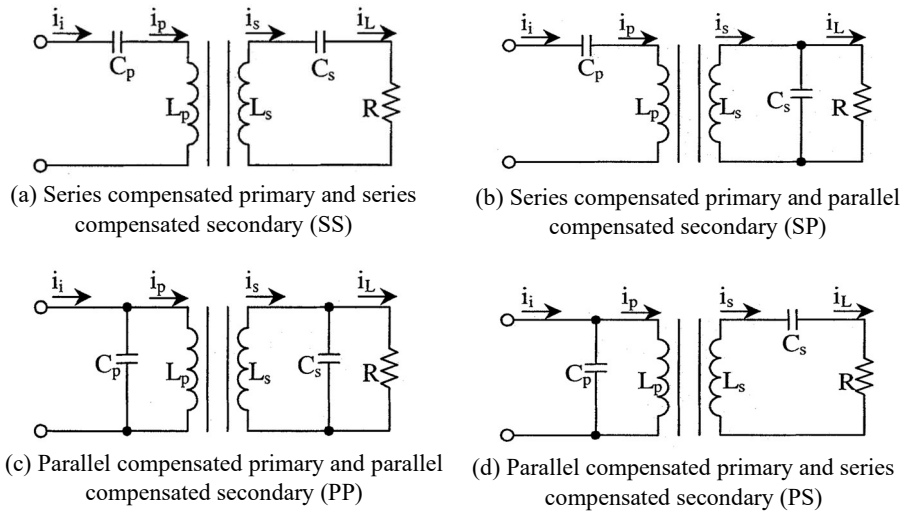

(a) Series compensated primary and series compensated secondary (SS)

(b) Series compensated primary and parallel compensated secondary (SP)

(c) Parallel compensated primary and parallel compensated secondary (PP)

(d) Parallel compensated primary and series compensated secondary (PS)

Figure 2-1: Four basic WPT topologies

The SS topology typically employs total compensation, and its compensation capacitance can remain constant, unaffected by variations in coupling and load. However, this topology may exhibit poorer output voltage regulation compared to others.

The SP topology typically requires more compensation because the circuit is prone to mistuning. This is due to the primary compensation capacitance in the SP topology being related to the degree of coupling. In this topology, the compensation capacitance needs to be adjusted based on the strength of the coupling, which can lead to circuit instability.

The PS and PP topologies require additional series inductors. These topologies often address issues that traditional two-element resonant topologies cannot, such as capacitance tolerance and voltage regulation [20].

2.4 Couplers

In WPT systems, the coupling structure plays a crucial role. It significantly influences the system's power, efficiency, and cost and has consistently been a focal point of research.

The coupling structure in WPT systems can be categorized into the transmitter (sender) side and the receiver (pickup) side. Generally, the transmitter is installed on the track to transmit energy, while the receiver is mounted on the bottom of the train to receive energy. This description primarily applies to systems that provide power to trains. However, in cases where the train needs to feed energy back to the grid, the distinctions between transmitters and receivers may not be as clear-cut.

Regardless of the specific structure, coils and magnetic cores are indispensable components. In the transmitter, coils generate an electromagnetic field to transmit energy; in the receiver, coils sense the electromagnetic field to receive power. Magnetic cores are primarily used to alter the path of electromagnetic field propagation, enabling a more significant portion of the field to couple between the transmitter and receiver coils. These cores are crucial for increasing transmission power and improving efficiency.

Regarding installation methods, current research is focused on two main approaches. The first involves installing the transmitter on a monorail or a third rail, which is well-suited for urban rail transit systems or maglev. In this thesis, it is called a monorail coupler. The second approach is to place the transmitter directly between the tracks, making it suitable for retrofitting older railway systems. In this thesis, it is called a planar coupler.

The monorail couplers described in references [23], [24], [25], [26], [27] feature a design where the transmitter side consists only of a conductive track or coil. In contrast, to increase the coupling factor , the receiver side employs multiple turns of wire coils, along with magnetic materials that either fully or partially surround the conductor on the transmitter side. This approach is relatively simple in structure and minimizes the use of magnetic materials.

In references [23, 24], Kacprzak and Elliott introduce the common E-pickup configuration used in monorail WPT systems, as shown in Figure 2-2 (a). They also discuss an S-pickup, which significantly enhances power transfer capability compared to a conventional E-shape by eliminating electromagnetic field cancellation without increasing the amount of ferrite used, as illustrated in Figure 2-2 (b). Additionally, [23] introduces some asymmetrical magnetic topologies suitable for monorail systems, including Z-shaped, λ-shaped, and U-shaped pickups.

In [25], Jiang introduces an M-shaped coupler structure, depicted in Figure 2-2 (c). This structure is combined with an LCL-S compensation topology, achieving an output of 180 kW. The efficiency of this design reached 95.5%.

In [28], Xu demonstrates a contactless transformer structure with a trapezoidal magnetic core, as shown in Figure 2-2 (d). The trapezoidal core's large opening, relative to its cross-sectional area, enhances the power transfer efficiency of the IPT system. Calculations and simulations indicate that this design can achieve an efficiency of 68.54% with a 30 kW capability.

In [26], Lee presents a removable and closed-shape dual-ring pickup, shown in Figure 2-2 (e). This proposed pickup improves the coupling efficiency of existing track systems by matching the core's flux path with the primary side's magnetic field pattern.

In [27], Moriki discusses a coaxial contactless power transmission system for electric railways, illustrated in Figure 2-2 (f). The transmitter side comprises the primary power supply cable, while the receiver side consists of a cylindrical magnetic core and a cylindrical conductor plate within the core.

These monorail coupling structures exhibit better coupling characteristics; however,

the movement range of the secondary coil is strictly limited, which can make their application inconvenient [29].

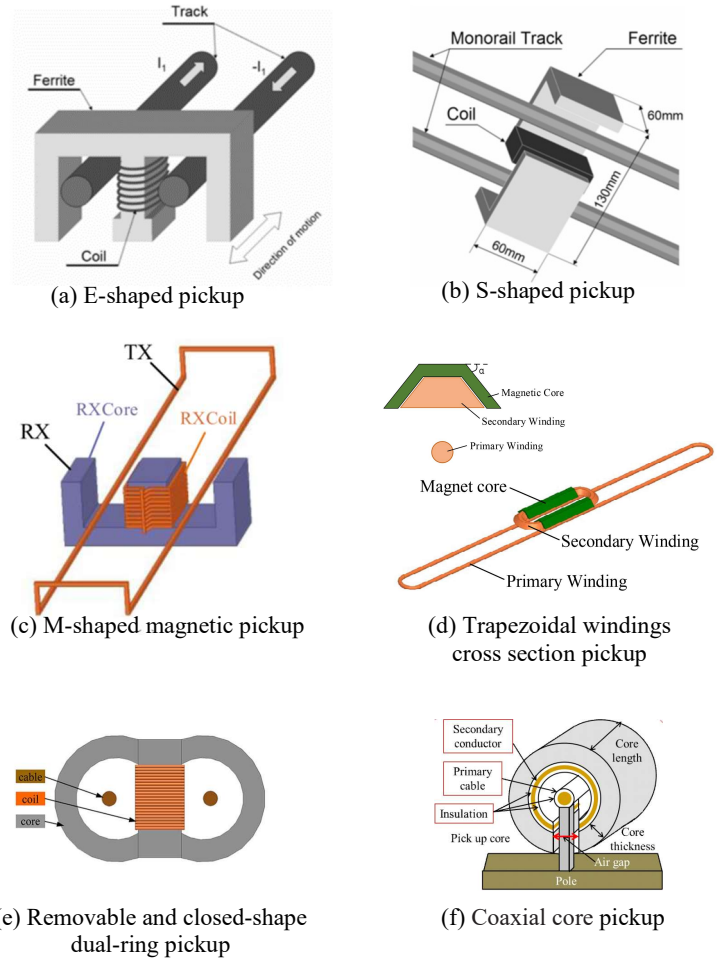

(a) E-shaped pickup

(b) S-shaped pickup

(c) M-shaped magnetic pickup

(d) Trapezoidal windings cross section pickup

(e) Removable and closed-shape dual-ring pickup

(f) Coaxial core pickup

Figure 2-2: Monorail couplers for WPT

In planar coupler structures, large-area coils are typically arranged to face each other. Magnetic materials are installed behind, alongside, or inserted into the coils to increase the coupling factor . This structure may require a significant number of magnetic materials, especially in the case of a long transmitter. To accommodate mobile applications, the coils on both the transmitter and receiver sides are typically designed in a rectangular shape.

In [30], Ukita introduces a figure-of-eight shaped coil coupler, as shown in Figure 2-3 (a). In this design, the magnetic core on the transmitter side (feeder cable) is eliminated to reduce costs, resulting in increased leakage flux. Despite this, the inductive coupling can provide a stable power supply even when the vehicle is in motion. The efficiency between the power source and the load resistor is 73%, with an output of 38.7 kW.

In [31], Park describes a 60kW-class WPT model and a ground power feeding line for a Wireless-Tram. As illustrated in Figure 2-3 (b), the transmitter side incorporates numerous ferrite cores to reduce leakage flux. However, the presence of a large amount of ferrite material increases both costs and installation complexity.

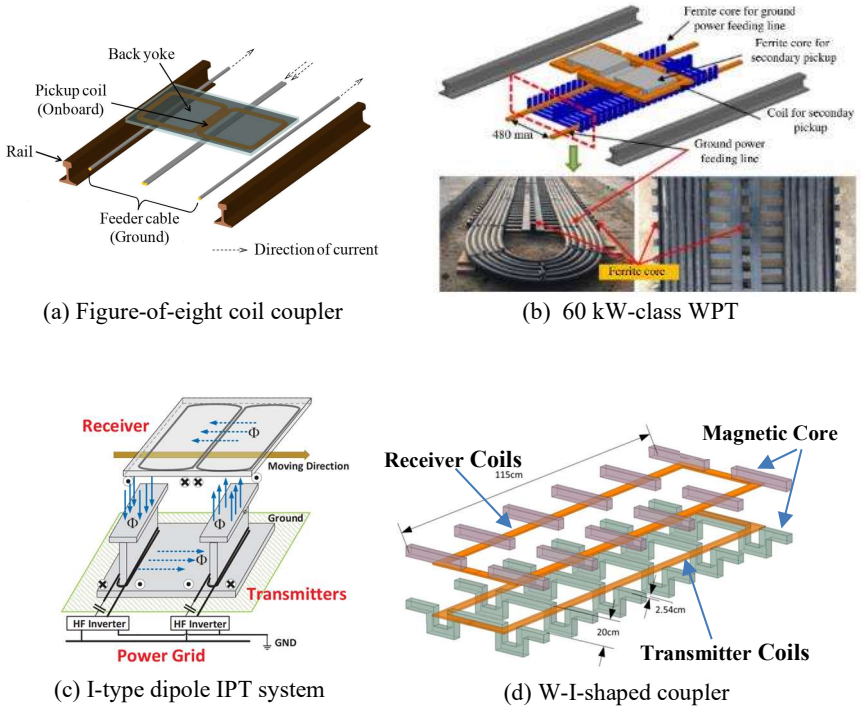

(a) Figure-of-eight coil coupler

(b) 60 kW-class WPT

(c) I-type dipole IPT system

(d) W-I-shaped coupler

Figure 2-3: Planar couplers for WPT

In [32], Wang proposes an arrangement of I-type ferrite cores for the on-track transmitter, depicted in Figure 2-3 (c). By exciting coil currents at a 180° phase shift, two I-type ferrite cores are magnetized as a dipole, allowing magnetic flux to pass from one

pole to another through the receiver coils. This creates a circulation path with the least reluctance.

In [9, 14], Xu develops an improved W-I-shaped ferrite core structure, shown in Figure 2-3 (d). The W-I type structure features a loose arrangement of ferrite cores on both the transmitter and receiver sides, significantly reducing material usage and costs. Despite its unique structural design, the system maintains a high coupling factor . The prototype has been validated at full power of 5 kW with a DC to DC efficiency of 92.5%.

Compared to monorail couplers, planar couplers are generally larger, more complex in structure, and more expensive. However, they offer a significant advantage in installation. Since the original rails do not require modification, installing the transmitter is much more straightforward; it simply needs to be placed between the rails. Additionally, because planar couplers can be completely sealed and powered on in sections, their safety is markedly improved.

2.5 Efficiency

Efficiency is a crucial metric in evaluating WPT performance. Enhancing WPT transmission efficiency helps to minimize electrical energy loss, thereby reducing carbon emissions and resource consumption, and lessening negative environmental impacts. Improved efficiency also translates to reduced heat dissipation requirements for the system, potentially simplifying system complexity and enhancing reliability. Moreover, higher efficiency in WPT transmission can lead to shorter charging times, yielding greater economic benefits. Collectively, these advantages will further promote the application and development of WPT.

Table 2-1: Comparison of WPT for railway applications

Organization	Topology	Power	Airgap	Efficiency	Year	Reference
KAIST	SS	27kW	20 cm	74%	2010	[33]
KAIST	SS	27kW	20 cm	74%	2011	[34]
KAIST	SS	79.5kW	20 cm	81.70%	2012	[35]
KAIST	SS	--	20 cm	91%	2013	[36]
The University of Auckland	LCL-T	6kW	--	94%	2013	[37]
KAIST	SS	100kW	26 cm	80%	2014	[38]
KAIST	SS	1MW	5 cm	82.70%	2015	[39]
KAIST	SS	9.5kW	20 cm	91%	2015	[40]
Southwest Jiaotong University	LCC	2.5kW	15 cm	92.58%	2018	[41]
Pathumwan Institute of Technology	SS	17.56kW	2.5 cm	69.14%	2019	[42]
Southwest Jiaotong University	Combined WPT	1.0kW	10 cm	90.97%	2019	[43]
Chongqing University of Technology	LCC-C	27.8kW	15 cm	93%	2019	[44]
Beijing Institute of Technology	LCC-S	7.85 kW	4 cm	92.0%	2020	[45]
KAIST	SS	12.7kW	23 cm	90.8%	2020	[46]
Harbin Institute of Technology	LCC-S	5kW	30 cm	82.70%	2020	[47]
Tsinghua University	LCL-S	180 kW	5.4 cm	95.5%	2021	[25]
UNC Charlotte	LCL-S	1.7 kW	12.7 cm	85.6%	2021	[14]
UNC Charlotte	LCL-S	5 kW	12.7 cm	92.5 %	2022	[9]

Table 2-1 presents basic information on selected railway wireless charging systems studied since 2010. The table reveals that, as research has progressed, the efficiency of WPT systems has gradually improved. Starting from an initial efficiency of 74% [33], it has now exceeded 92% in later studies [41], [45], [9]. This trend also indicates that research on railway WPT is receiving increasing attention.

2.6 Dynamic Analysis

Due to the strong universality of dynamic charging in the EV and railway sectors, this section includes some relevant research in the field of EVs.

2.6.1 Output Voltage Fluctuations

The output remains stable during static charging, as the receiver and transmitter are relatively stationary. However, during dynamic charging processes, the relative position between the receiver and transmitter undergoes dramatic changes along the railway direction. Simultaneously, vibrations can induce variations in the vertical air gap and lead to lateral misalignment, causing fluctuations in the system's output voltage and current. Additionally, certain inherent characteristics of the coupler can introduce significant fluctuations.

Research by [48] indicates that a setup involving multiple E-core coil transmitters and a single E-core Long receiver yields a voltage output with a wide fluctuation range. In [49], simulations demonstrate that the area covered by the coils plays a crucial role in the coupling factor, with square coils being the optimal choice. They design an array of twelve transmitter coils, over which an inferred receiver coil moves, achieving constant power transmission under the given conditions. To achieve stable output during dynamic charging, [47] proposes a narrow-rail three-phase magnetic coupler that integrates the advantages of conventional three-phase meander-type couplers and conventional single-phase couplers with alternately arranged poles for EV dynamic wireless charging. Experimental results show that the output voltage fluctuation remains within ±2.5% during dynamic charging. Research by [50] finds that power pulsations in the DD/Q transmitter and DDQ receiver coils of the WPT model can be observed because the summation of mutual inductance between adjacent transmitters is not perfectly identical. Research by [51] proposes an n-type power supply rail and a dual-phase coil receiver. Compared with the I-type magnetic pole, the n-type pole can reduce magnetic core usage and slightly improves transmission

and coupling performance. The dual-phase coil receiver also addresses the significant voltage fluctuation observed with single-phase configurations.

2.6.2 Electromagnetic Field Radiation

WPT systems rely on electromagnetic fields to transmit energy, which inevitably raises concerns about electromagnetic interference (EMI) in the surrounding environment.

In [47], a tripolar WPT system is proposed for railway applications to mitigate electromagnetic field (EMF) emissions. Compared to conventional long straight WPT systems, the proposed system partially addresses the issue of electromagnetic radiation. Reference [52] conducts EMF measurements around a railway WPT system and suggests a shielding design to reduce EMF leakage. The results indicate that the proposed method significantly decreases EMF density and complies with ICNIRP 1998 and ICNIRP 2010 standards at specific distances. In [53], EMF and EMI measurements are performed at various locations where passengers could be present in a 1-megawatt (MW) WPT light rail transit system. The highest measured EMF value is 2.41 μT, below the international guideline value of 6.25 μT in ICNIRP 1998. In [51], EMF measurements indicate values under 27 μT at a distance of 100 cm from the transmitter.

2.6.3 Segmented Transmitter Power Supply

In railway systems, WPT systems installed in the middle of railway tracks pose potential safety concerns due to high voltage and strong electromagnetic fields when energized. Both factors can present safety hazards for humans and animals. Additionally, the system requires shorter transmitter coil designs from an efficiency standpoint. Therefore, in practical applications, segmented coils are the most ideal structure. Consequently, a reasonable control logic is to power up the transmitter under the receiver's

bottom only when a train passes. This requires knowledge of the train's position. When a vehicle transitions from one transmitter to another, the transmitter coils switch accordingly to ensure continuous energy supply.

In [54], the authors investigate a method for detecting a vehicle based on tags. The position data stored in these tags can be read by a reader placed at the bottom of the vehicle. Hwang introduces an axle counter designed to detect passing train wheels by monitoring changes in the magnetic field generated by the train wheels in a receiving coil [55]. However, this approach might not be suitable for use with a WPT system, as the WPT system could produce electromagnetic interference and affect the performance of the axle counter. Therefore, they propose an alternative train detection device called the pickup coil counter (PCC). The PCC can detect the pickup coil onboard the train.

2.6.4 Position of Charging

When considering the entire railway line as a research objective, the issue of site selection for dynamic charging also arises. Reference [56] conducts tests on transmitter distribution methods, which include nine models featuring both continuous and discontinuous wireless charging lanes. They find that dispersing transmitters in areas where the train's speed is relatively slow, such as start-up and deceleration zones, can yield the maximum cumulative energy.

In [12], Ahmad proposes a method for assessing the state of charge (SoC) of hybrid locomotives along the track and determines the position of charging stations on a train network, based on simulation. These research findings provide valuable insights for the future applications of WPT in railway systems.

CHAPTER 3: WPT DESIGN FOR LOCOMOTIVES

3.0 Introduction

This chapter introduces a WPT system for locomotives, comprising the LCL-S compensation topology and the W-I-shaped coupler. The LCL-S compensation topology is renowned for enhancing power transfer capacity and reducing voltage and current stresses, making it especially suitable for loosely coupled WPT systems. The W-I-shaped coupler structure is adopted for its high material utilization efficiency, which reduces the use of core materials.

In addition, this chapter introduces the material effect factor (MEF) as a metric for comparing various coupler designs in terms of material utilization efficiency. The results underscore the W-I-shaped coupler design as having the highest MEF, thereby significantly reducing core material usage.

3.1 System Structure

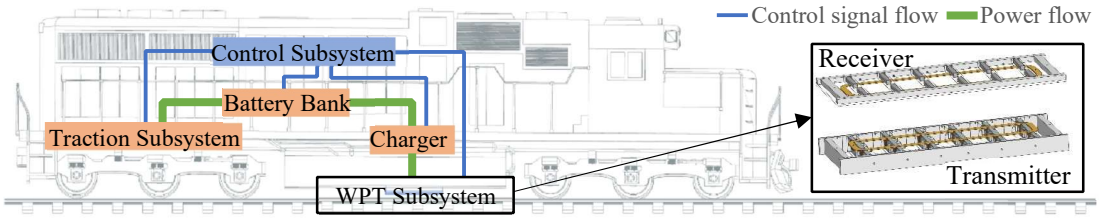

Figure 3-1: Simplified concept of locomotive with a WPT system

Figure 3-1 depicts a simplified system structure of the locomotive with WPT, consisting of a control subsystem, a traction subsystem, a battery bank, a charger, and the WPT subsystem. The WPT subsystem includes a transmitter and a receiver. The transmitter is installed between tracks, and the receiver is installed under the underbelly of the

locomotive. Power is transferred from the transmitter to the receiver wirelessly and sent to the charger. The charger charges the battery bank, and the battery bank drives the traction subsystem. The control subsystem collects signals from other subsystems and coordinates the operation of each subsystem. This thesis only focuses on the WPT subsystem.

3.2 LCL-S Compensation Topology of WPT

3.2.1 LCL-S Compensation Topology

The LCL-S compensation topology, in which the "LCL" denotes the inductor-capacitor-inductor structure of the primary side and "S" represents the secondary capacitor series with the secondary winding. It is suitable for wireless charging applications based on efficiency, voltage, and current stress. In references [9, 14], Xu employes this topology to enhance the power transfer capability of the system and to reduce the volt-amps rating on both the source and load sides in a loosely coupled WPT system.

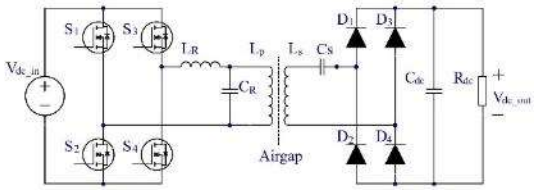

Figure 3-2: LCL-S compensation topology

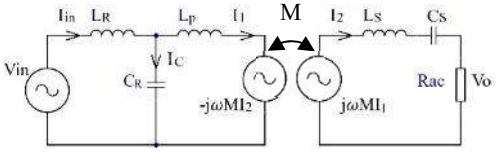

Figure 3-3: LCL-S compensation equivalent circuit

The LCL-S compensation topology presented in this paper is illustrated in Figure 3-2. On the primary/transmitter side, four N-channel metal-oxide-semiconductor field-effect transistors (MOSFETs, labeled S1 to S4) are employed to generate a high-frequency alternating current (AC) of 85 kHz. On the secondary/receiver side, an H-bridge consisting of diodes D1 to D4 is used to rectify the AC back to direct current (DC).

Figure 3-3 shows the equivalent circuit, incorporating design constraints such as $\omega L_R = \frac{1}{\omega C_R}, L_R = L_p,\ \omega L_S = \frac{1}{\omega C_S}$. Based on these constraints, the voltage and current can

be derived as follows:

$$V_{in} = I_{in} j\omega L_R + (I_{in} - I_1)\frac{1}{j\omega C_R} = I_{in}\left(j\omega L_R + \frac{1}{j\omega C_R}\right) - I_1\frac{1}{j\omega C_R}$$

$$= -I_1\frac{1}{j\omega C_R} \quad (1)$$

$$V_O = I_1 j\omega M + I_2\left(j\omega L_S + \frac{1}{j\omega C_S}\right) = I_1 j\omega M \quad (2)$$

so that,

$$I_1 = -V_{in} j\omega C_R = V_{in}\frac{1}{j\omega L_R} \quad (3)$$

also,

$$V_O = V_{in}\omega^2 M C_R = V_{in} M\frac{1}{L_R} \quad (4)$$

According to (3), the current I_1 only relates to the input voltage *Vin*, the angular speed ω at switching frequency, and capacitor C_R or inductor L_R. According to (4), the output voltage V_O is load (R_{ac}) independent, where M is the mutual inductance of transmitter and receiver.

3.2.2 Multiple-Transmitter and Single-Receiver LCL-S Compensation Topology

This thesis introduces a multiple-transmitter and single-receiver (MTSR) LCL-S compensation topology, which is employed to dynamically analyze WPT for railway applications. This topology is illustrated in Figure 3-4 which includes both transmitter and receiver sides. On the transmitter side, three transmitters with a half LCL-S compensation topology are connected in parallel to the same DC source. Each transmitter employs four N-channel MOSFETs (Sx1 to Sx4, where "x" represents the number of the transmitter) to generate a high-frequency AC of 85 kHz. All three transmitters use the same set of gate

drive signals, ensuring synchronous AC generation. On the receiver side, a Silicon Carbide (SiC) diode full-bridge power module (D1 to D4) is utilized to rectify AC back to DC. These chips, characterized by low on-resistance and low forward voltage, enhance the system with improved power density and efficiency. This new topology not only inherits the advantages of the original LCL-S compensation topology but also facilitates dynamic experiments.

3.3 W-I-shaped Coupler of WPT

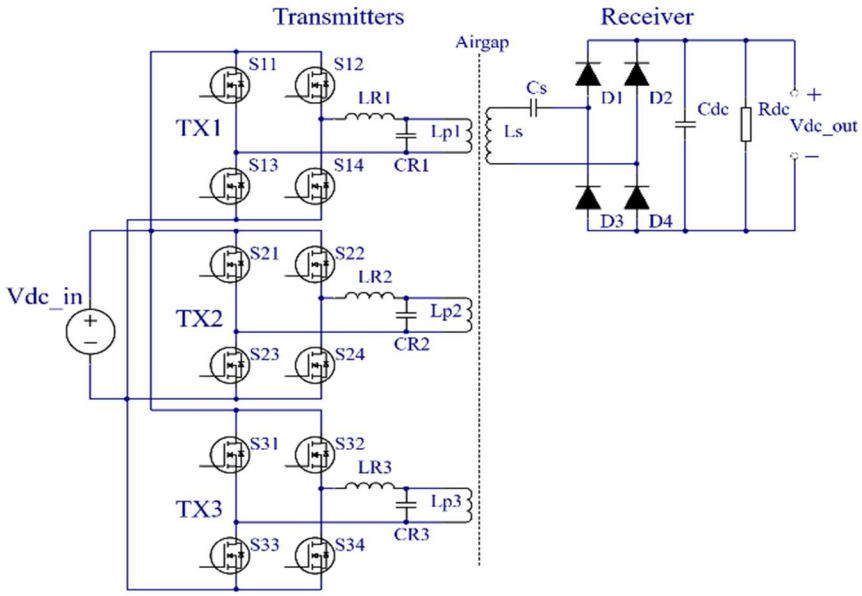

Figure 3-4: Multiple-transmitter and single-receiver LCL-S compensation topology

3.3.1 W-I-shaped Coupler Structure

In this thesis, the W-I-shaped coupler, as proposed by [9, 14], is adopted. Figure 3-5 shows a model depicting the structure of the coupler. The upper part represents the receiver (Rx), and the lower part is the transmitter (Tx). For the receiver, there are six pairs of I-shaped cores alongside the receiver coils. Conversely, the transmitter comprises six W-shaped cores and the transmitter coils. The core material is Ferroxcube 3C90, which has a relative permeability of 2300 at 25°C and is suitable for use at frequencies up to 200 kHz.

The coils are made of 1500/38 Litz wire, consisting of 1500 strands of 38 AWG (0.1mm) wires, designed to alleviate the skin-effect and reduce conduction loss. The air gap of the coupler is designed to be 5 inches (12.7 cm).

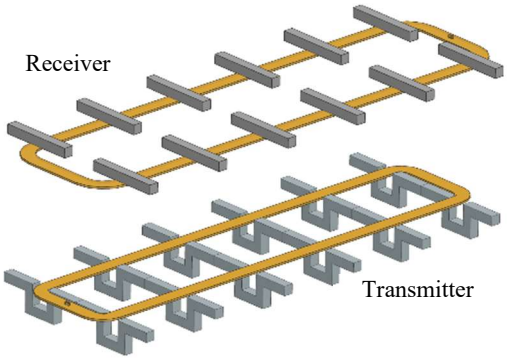

Figure 3-5: W-I-shaped coupler

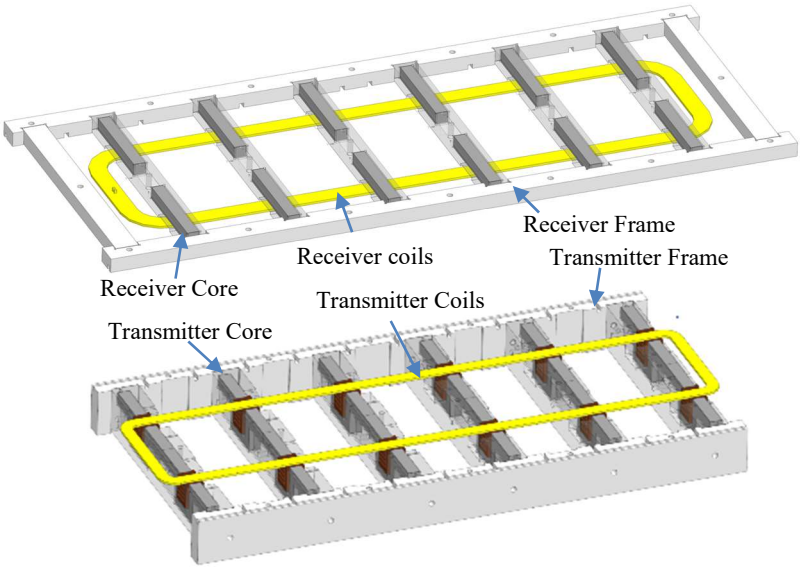

Figure 3-6: W-I-shaped coupler with frames

Figure 3-6 displays the coupler equipped with frames. Both the receiver and transmitter frames are composed of plastic bars, which are connected using aluminum fasteners. Notches are carved into plastic bars to accommodate the magnetic cores. These ladder-like assemblies provide support for the coils and cores on both the receiver and transmitter sides.

3.3.2 Coupling Factor

The coupling factor, denoted as *k*, is a parameter used to describe the coupling between two coils or transformers in an electrical or magnetic circuit. It is closely related to the transmission capability in a WPT system. In this thesis, the *k* value of the W-I-shaped coupler is determined as follows.

Figure 3-7 illustrates the magnetic equivalent circuit of the W-I coupler.

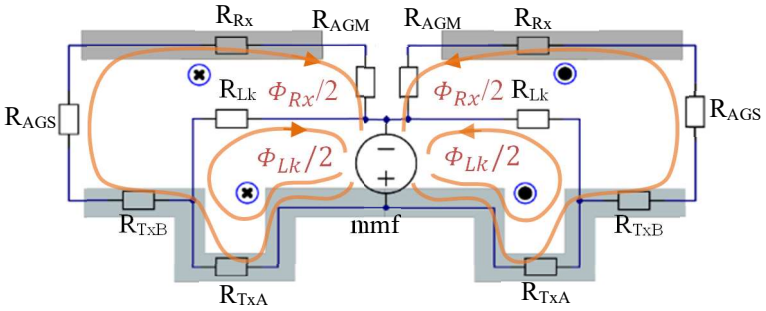

Figure 3-7: W-I-shaped coupler magnetic equivalent circuit

The flux received by the receiver Φ_{Rx} and the leakage flux Φ_{Lk} can be represented by the following equations:

$$\frac{\Phi_{Rx}}{2} = \frac{mmf\dfrac{R_{Lk}}{R_{Lk}+(R_{AGM}+R_{Rx}+R_{AGS}+R_{TxB})}}{R_{TxA}+\dfrac{R_{Lk}(R_{AGM}+R_{Rx}+R_{AGS}+R_{TxB})}{R_{Lk}+(R_{AGM}+R_{Rx}+R_{AGS}+R_{TxB})}} \tag{5}$$

$$\frac{\Phi_{Lk}}{2} = \frac{mmf\dfrac{R_{AGM}+R_{Rx}+R_{AGS}+R_{TxB}}{R_{Lk}+(R_{AGM}+R_{Rx}+R_{AGS}+R_{TxB})}}{R_{TxA}+\dfrac{R_{Lk}(R_{AGM}+R_{Rx}+R_{AGS}+R_{TxB})}{R_{Lk}+(R_{AGM}+R_{Rx}+R_{AGS}+R_{TxB})}} \tag{6}$$

Where *mmf* is the magnetomotive force generated in the transmitter coils, R_{AGM} is the magnetic reluctance of the middle air gap, R_{AGS} is the magnetic reluctance of the side air gap, R_{Rx} is the magnetic reluctance of the receiver cores, R_{Lk} is the leakage reluctance, R_{TxA} and R_{TxB} are the magnetic reluctance of the transmitter cores.

The k can be expressed as follow,

$$k = \frac{\Phi_{Rx}}{\Phi_{Rx} + \Phi_{Lk}} = \frac{R_{Lk}}{R_{Lk} + (R_{AGM} + R_{Rx} + R_{AGS} + R_{TxB})} \tag{7}$$

In (7), R_{Rx} and R_{TxB} depend on the distribution of cores. Since the distribution of the core has been determined, these parameters can be considered as constant.

In addition, for a uniform magnetic circuit the reluctance R can be calculated with the following formula,

$$R = \frac{l}{\mu_0 \mu_r A} \tag{8}$$

Where l is the length of the magnetic circuit, μ_0 is the vacuum permeability, μ_r is the relative magnetic permeability of the material, and A is the cross-sectional area of the magnetic circuit.

Since the relative magnetic permeability of the core material is 2300 (Ferroxcube 3C90) and is much higher than that of the air, which is 1, according to (8), $R_{AGM} + R_{AGS} \gg R_{Rx} + R_{TxB}$ and (7) can be approximated as follow,

$$k \approx \frac{1}{1 + \frac{R_{AGM} + R_{AGS}}{R_{Lk}}} \tag{9}$$

Also, because R_{AGM} and R_{AGS} are all directly relative to the air gap, they can be combined as one parameter $R_{AG} = R_{AGM} + R_{AGS}$. Then, equation (9) is simplified to,

$$k \approx \frac{1}{1 + \frac{R_{AG}}{R_{Lk}}} \tag{10}$$

Since the structure of the cores being fixed, and R_{Lk} is relatively constant, therefore, the value of k depends on R_{AG}, that is the air gap. An increase in the air gap leads to a decrease in the value of k.

According to the experiments, which will be detailed below, when the transmitter and receiver are perfectly aligned with each other, the maximum value of *k* is found to be 0.2327. At this point,

$$R_{AG} = 3.2974\, R_{Lk} \tag{11}$$

Equation (11) can be utilized to estimate the relationship between the coupling factor and the misalignment distance. Consequently, it can be predicted that the *k* value will be at its maximum when the transmitter cores are aligned with the receiver cores. Conversely, the *k* value will decrease when there is misalignment between the transmitter and receiver cores.

In this WPT system, another expression of coupling factor is, $k = \frac{M}{\sqrt{L_p L_s}}$, where L_p is the inductance of the primary side coils, L_s is the inductance of secondary side coils, and M is the mutual inductance of L_p and L_s. Therefore, (4) can be modified to,

$$V_O = kV_{in}\omega^2\sqrt{L_p L_s}C_R, \text{or } V_O = \frac{kV_{in}\sqrt{L_p L_s}}{L_R} \tag{12}$$

From (12), the conclusion that can be drawn is that during static charging when k remains constant, the output voltage V_O is linearly related to the input voltage V_{in}.

3.3.3 Coupling Factor During Misalignment

When calculating the coupling factor for misalignment, three assumptions are made:

Firstly, due to the dispersed distribution of magnetic cores, the electromagnetic field tends to be relatively dense around the cores. Precisely calculating this based on actual conditions is very difficult and not necessary. Therefore, it is assumed that the electromagnetic fields of the transmitter and receiver are uniform.

Secondly, as all coils are handcrafted, there will inevitably be slight differences in their inductance values. However, these differences are considered negligible. Thus, it is assumed that all transmitter coils have equal inductance values.

Thirdly, when the train travels on the tracks, there is almost no displacement in the direction perpendicular to the tracks. Hence, it is assumed that misalignments exist only along the direction of the tracks.

The parameters for calculating k are illustrated in Figure 3-8. In the figure, L_{RxC_lo} represents the outer length of the receiver coils; L_{RxC_li} is the inner length of the receiver coils; L_{TxC_lo} is the outer length of transmitter coils; L_{TxC_li} is the inner length of transmitter coils; D_{mis} is the distance between the centers of the receiver and the first transmitter; D_{TT} is the distance between the outer edges of the two transmitter coils.

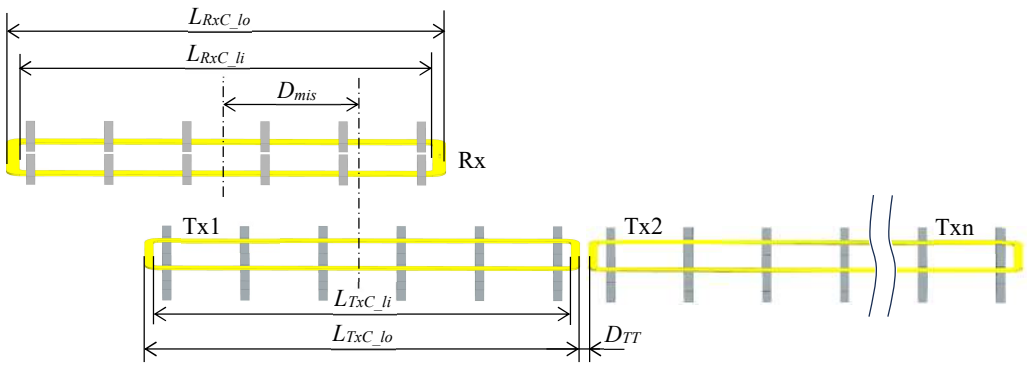

Figure 3-8: Parameters for calculating *k*

For a WPT system with one receiver (Rx) and N transmitters (Tx1 to TxN), the calculation process can be divided into five stages: (1) Approaching stage, (2) Falling stage, (3) Plain stage, (4) Rising stage, and (5) Leaving stage. These five stages are depicted in Figure 3-9 (a), and the position of the receiver at each stage is shown in Figure 3-9 (b).

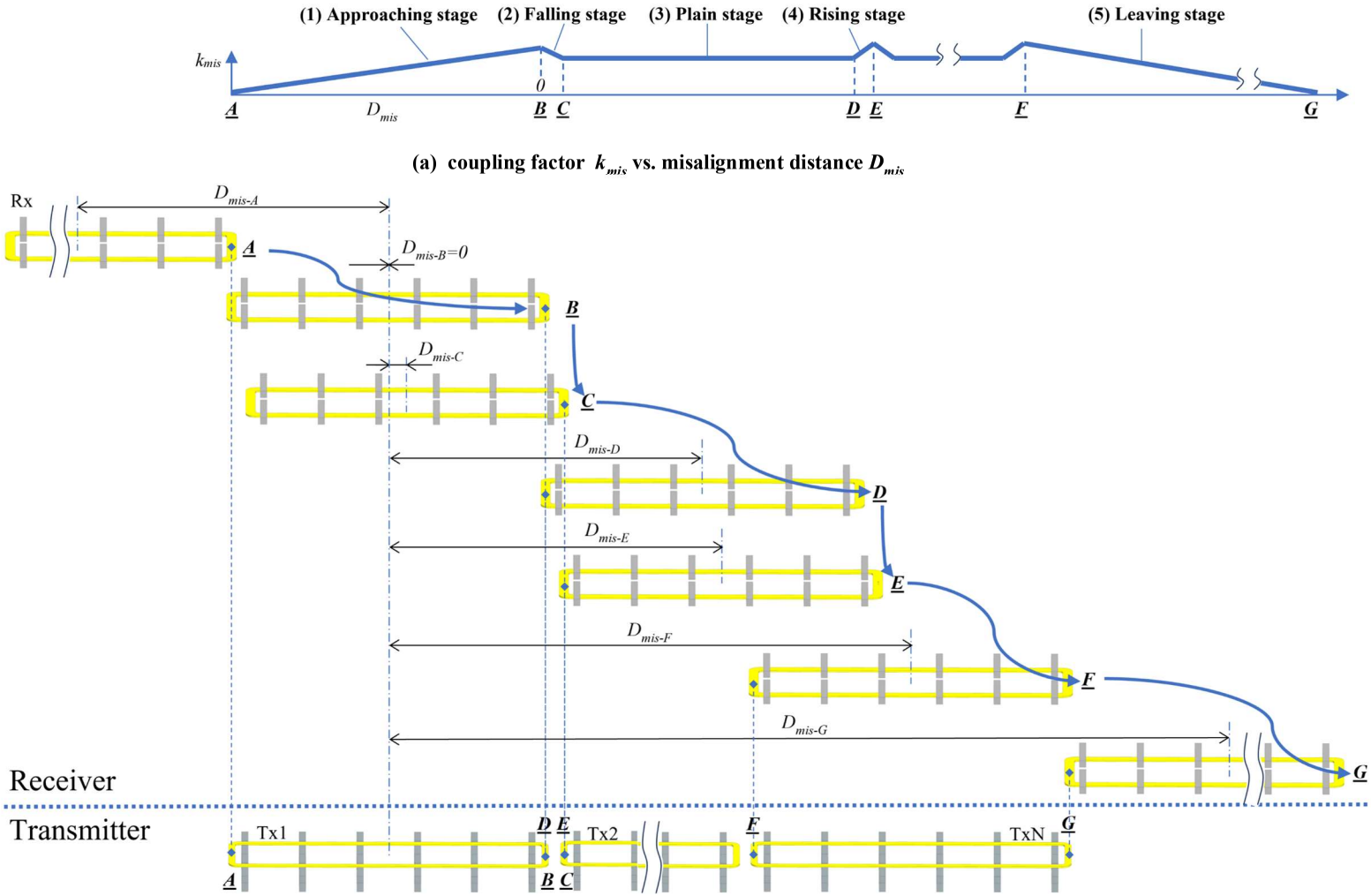

(a) coupling factor k_{mis} vs. misalignment distance D_{mis}

(b) Receiver's positions at five stages

Figure 3-9: Five stages for calculating *k* during misalignment

At the approaching stage, from A to B, the receiver is on the left side of the first transmitter Tx1 and the misalignment value is negative. The misalignment distance D_{mis} is from $D_{mis\text{-}A}$ to $D_{mis\text{-}B}$, corresponding to the range of $-\frac{L_{Tx\ lo}+L_{TxC_{li}}}{4}-\frac{L_{RxC_{lo}}+L_{Rx\ li}}{4}<D_{mis}\leq 0$. The coupling factor k_{mis} can be calculated by (13), where k_{alg} is the coupling factor value when one transmitter aligns with the receiver.

$$k_{mis}=k_{alg}\left(1+\frac{2D_{mis}}{L_{RxC_{lo}}+L_{Rx\ li}}\right),$$

$$if\ \ -\frac{L_{TxC_{lo}}+L_{Tx\ li}}{4}-\frac{L_{RxC_{lo}}+L_{Rx\ li}}{4}<D_{mis}\leq 0 \qquad (13)$$

At the falling stage, from B to C, the receiver is over the transmitters and the misalignment value is positive. The misalignment distance D_{mis} is from $D_{mis\text{-}B}$ to $D_{mis\text{-}C}$, corresponding to the range of $(n-1)\left(L_{TxC_{lo}}+D_{TT}\right)<D_{mis}\leq(n-1)\left(L_{TxC_{lo}}+D_{TT}\right)+D_{TT}+\frac{L_{TxC_{lo}}-L_{TxC_{li}}}{2}$. The coupling factor k_{mis} can be calculated by (14):

$$k_{mis}=k_{alg}\left(1-\frac{2\left(D_{mis}-(n-1)\left(L_{TxC_{lo}}+D_{TT}\right)\right)}{L_{RxC_{lo}}+L_{RxC_{li}}}\right),$$

$$if\ (n-1)\left(L_{TxC_{lo}}+D_{TT}\right)<D_{mis}$$

$$\leq(n-1)\left(L_{TxC_{lo}}+D_{TT}\right)+D_{TT}+\frac{L_{TxC_{lo}}-L_{TxC_{li}}}{2} \qquad (14)$$

Where n is the No. of the transmitter, and $n\in\{1,2,\cdots,N-1\}$, N is the total number of transmitters.

At the plain stage, from C to D, the receiver is over the transmitters and the misalignment value is positive. The misalignment distance D_{mis} is from $D_{mis\text{-}C}$ to $D_{mis\text{-}D}$, corresponding to the range of $(n-1)\left(L_{Tx\ lo}+D_{TT}\right)+D_{TT}+\frac{L_{TxC_{lo}}-L_{Tx\ li}}{2}<D_{mis}\leq$

$(n-1)\left(L_{TxC_{lo}}+D_{TT}\right)+\frac{L_{RxC_{lo}}+L_{RxC_{li}}}{4}+\frac{L_{TxC_{lo}}+L_{TxC_{li}}}{4}$. At this stage, the k_{mis} is a constant value and can be calculated by (15):

$$k_{mis}=k_{alg}\left(1-\frac{2\left(D_{TT}+L_{TxC_{lo}}-L_{Tx\ \ li}\right)}{L_{RxC_{lo}}+L_{RxC_{li}}}\right),$$

$$if\ (n-1)\left(L_{TxC_{lo}}+D_{TT}\right)+D_{TT}+\frac{L_{TxC_{lo}}-L_{TxC_{li}}}{2}<D_{mis}$$

$$\leq(n-1)\left(L_{TxC_{lo}}+D_{TT}\right)+\frac{L_{RxC_{lo}}+L_{RxC_{li}}}{4}+\frac{L_{TxC_{lo}}+L_{Tx\ \ li}}{4} \qquad (15)$$

Where n is the No. of the transmitter, and $n\in\{1,2,\cdots,N-1\}$, N is the total number of transmitters.

At the plain stage, from D to E, the receiver is over the transmitters and the misalignment value is positive. The misalignment distance D_{mis} is from $D_{mis\text{-}D}$ to $D_{mis\text{-}E}$, corresponding to the range of $(n-1)\left(L_{TxC_{lo}}+D_{TT}\right)+\frac{L_{Rx\ \ lo}+L_{RxC_{li}}}{4}+\frac{L_{TxC_{lo}}+L_{TxC_{li}}}{4}<D_{mis}\leq(n-1)\left(L_{TxC_{lo}}+D_{TT}\right)+\frac{L_{RxC_{lo}}+L_{RxC_{li}}}{4}+\frac{L_{TxC_{lo}}+L_{Tx\ \ li}}{4}+\frac{L_{TxC_{lo}}-L_{TxC_{li}}}{2}+D_{TT}$. The misalignment coupling factor k_{mis} can be calculated by (16):

$$k_{mis}=k_{alg}\left(1+\frac{2\left(D_{mis}-(n-1)\left(L_{TxC_{lo}}+D_{TT}\right)\right)}{L_{RxC_{lo}}+L_{RxC_{li}}}\right),$$

$$if\ (n-1)\left(L_{TxC_{lo}}+D_{TT}\right)+\frac{L_{RxC_{lo}}+L_{RxC_{li}}}{4}+\frac{L_{TxC_{lo}}+L_{TxC_{li}}}{4}<D_{mis}$$

$$\leq(n-1)\left(L_{TxC_{lo}}+D_{TT}\right)+\frac{L_{RxC_{lo}}+L_{RxC_{li}}}{4}+\frac{L_{TxC_{lo}}+L_{TxC_{li}}}{4}$$

$$+\frac{L_{TxC_{lo}}-L_{TxC_{li}}}{2}+D_{TT} \qquad (16)$$

Where n is the No. of the transmitter, and $n\in\{1,2,\cdots,N-1\}$, N is the total number of transmitters.

From E to F, the k_{mis} repeats the stage from B to E periodically.

At the plain stage, from F to G, the receiver is over the last transmitter Tx*N,* and the misalignment value is positive. The misalignment D_{mis} is from $D_{mis\text{-}F}$ to $D_{mis\text{-}G}$, corresponding to the range of $(N-2)\left(L_{TxC_{lo}}+D_{TT}\right)+\frac{L_{RxC_{lo}}+L_{RxC_{li}}}{4}+\frac{L_{TxC_{lo}}+L_{TxC_{li}}}{4}+\frac{L_{TxC_{lo}}-L_{TxC_{li}}}{2}+D_{TT}<D_{mis}\leq(N-2)\left(L_{TxC_{lo}}+D_{TT}\right)+\frac{L_{RxC_{lo}}+L_{Rx\ li}}{4}+\frac{3(L_{TxC_{lo}}+L_{TxC_{li}})}{4}+\frac{L_{TxC_{lo}}-L_{TxC_{li}}}{2}+D_{TT}$. The misalignment coupling factor k_{mis} can be calculated by (17):

$$k_{mis}=k_{alg}\left(1-\frac{2\left(D_{mis}-(N-1)\left(L_{TxC_{lo}}+D_{TT}\right)\right)}{L_{RxC_{lo}}+L_{RxC_{li}}}\right),$$

$$if\ (N-2)\left(L_{TxC_{lo}}+D_{TT}\right)+\frac{L_{TxC_{lo}}+L_{TxC_{li}}}{4}+\frac{L_{TxC_{lo}}-L_{TxC_{li}}}{2}+D_{TT}+\frac{L_{Rx\ \ lo}+L_{RxC_{li}}}{4}$$

$$<D_{mis}$$

$$\leq(N-2)\left(L_{TxC_{lo}}+D_{TT}\right)+\frac{L_{RxC_{lo}}+L_{RxC_{li}}}{4}+\frac{3(L_{TxC_{lo}}+L_{TxC_{li}})}{4}$$

$$+\frac{L_{TxC_{lo}}-L_{TxC_{li}}}{2}+D_{TT} \tag{17}$$

where N is the total number of transmitters.

These equations can be used to simulate the WPT modules. For a STSR WPT with the parameters listed in Table 3-1, combined these formulas with (12), the output voltage V_O can be calculated by the step function (18).

$$V_O=\begin{cases}0.3639\left(1+\frac{D_{mis}}{48}\right)V_{in}, & if\ -48<D_{mis}\leq 0\\ 0.3639\left(1-\frac{D_{mis}}{48}\right)V_{in}, & if\ 0<D_{mis}\leq 48\end{cases} \tag{18}$$

Table 3-1: MTSR coupler dimensional parameters

Parameter	Symbol	Value
Rx Coils Outer Length	L_{RxC_lo}	49.5”/125.73cm
Rx Coils Inner Length	L_{RxC_li}	46.5”/118.11cm
Tx Coils Outer Length	L_{TxC_lo}	49”/124.46cm
Tx Coils Inner Length	L_{TxC_li}	47”/119.38cm
Distance Between Transmitters	D_{TT}	0
Tx3 Capacitor	C_{R3}	48.90 *n*F
Rx Inductor	L_s	175.30 uH
Rx Capacitor	C_S	20 *n*F
Tx Inductor	L_p, L_R	71.70 *u*H
Aligned Coupling Factor	k_{alg}	0.2327

For an input voltage of 705 V DC, the output voltages at different misalignments expected are shown in Figure 3-10, the maximum output voltage is 256.55 V.

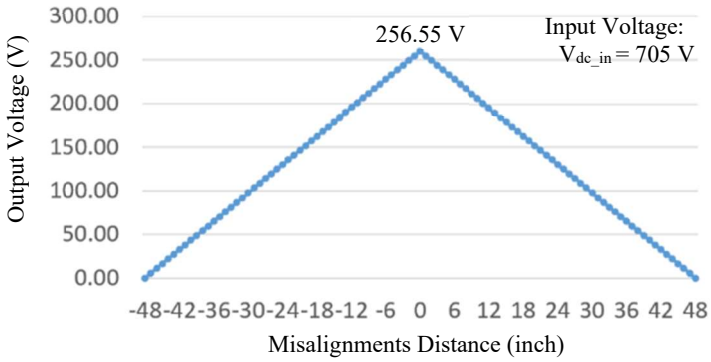

Figure 3-10: Calculated output voltages under different misalignments

For a N-transmitter and one-receiver WPT system, the k_{mis} can be calculated by (19).

$$k_{mis} = \begin{cases} 0.2327\left(1+\dfrac{D_{mis}}{48}\right), & if \ -48 < D_{mis} \le 0 \\ 0.2327\left(1-\dfrac{D_{mis}-49n+49)}{48}\right), & if\ 49n-49 < D_{mis} \le 49n-48 \\ 0.2279, & if\ 49n-48 < D_{mis} \le 49n-1 \\ 0.2327\left(1+\dfrac{D_{mis}-49n+49}{48}\right), & if\ 49n-1 < D_{mis} \le 49n \\ 0.2327\left(1-\dfrac{D_{mis}-49N+49}{48}\right), & if\ 49N-49 < D_{mis} \le 49N-1 \end{cases} \quad (19)$$

Where $n \in \{1,2,\dots N-1\}$ and N is the total number of transmitters, D_{mis} is the

distance between the receiver's and the first transmitter's centers.

Combined (19) with (12), (20) can be used to calculate the output voltages.

$$V_O = \begin{cases} 0.3639\left(1+\dfrac{D_{mis}}{48}\right)V_{in}, & if \ -48 < D_{mis} \le 0 \\ 0.3639\left(1-\dfrac{D_{mis}-49n+49)}{48}\right)V_{in}, & if\ 49n-49 < D_{mis} \le 49n-48 \\ 0.3562V_{in}, & if\ 49n-48 < D_{mis} \le 49n-1 \\ 0.3639\left(1+\dfrac{D_{mis}-49n+49}{48}\right)V_{in}, & if\ 49n-1 < D_{mis} \le 49n \\ 0.3639\left(1-\dfrac{D_{mis}-49N+49}{48}\right)V_{in}, & if\ 49N-49 < D_{mis} \le 49N-1 \end{cases} \quad (20)$$

Where V_O is the output voltage, V_{in} is the input voltage, $n \in \{1,2,\dots N-1\}$ and N is the total number of transmitters, D_{mis} is the distance between the receiver's and the first transmitter's centers.

For a three-transmitter and one-receiver model with an input voltage of 705 V DC, the calculated output voltages are shown in Figure 3-11.

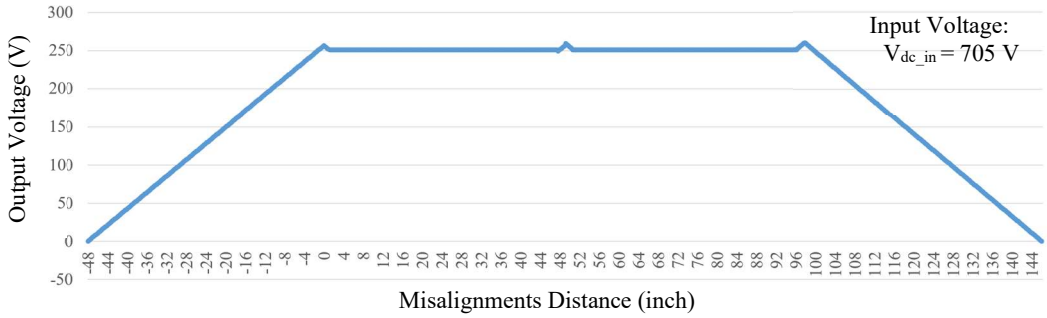

Figure 3-11: Calculated output voltages for three-transmitter and one-receiver WPT

3.3.4 Core MEF

In [14], four types of coupler designs are compared, as displayed in Figure 3-12. These designs include (a) Aligned I-type[34], (b) Paralleled I-type [32], (c) U-U Shaped [39], and (d) W-I-shaped [14]. Table 3-2 provides a list of the volume of core, coupling factor , and MEF of each design.

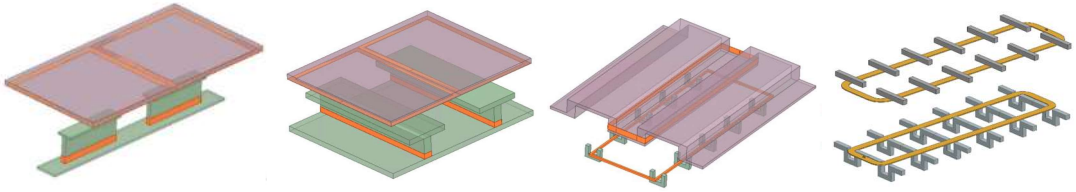

(a) Aligned I-type (b) Paralleled I-type (c) U-U Shaped (d) W-I Shaped

Figure 3-12: Four coupler designs

Table 3-2: Comparison of four coupler designs

Type	Volume of core: V_{core}	Coupling factor : k	Material effect factor: MEF
Aligned I-type	12860 cm^3	0.174	$1.353\times10^{-5}/cm^3$
Paralleled I-type	69600 cm^3	0.345	$4.957\times10^{-6}/cm^3$
U-U Shaped	30270 cm^3	0.194	$6.409\times10^{-6}/cm^3$
W-I Coupler	4709 cm^3	0.2327	$4.942\times10^{-5}/cm^3$

To compare the effect of using core materials, the MEF is introduced. It is calculated by dividing the coupling factor k by the volume of the core V_{core}. The MEF indicates the power transmission capacity per unit volume of core material for a coupler design, thereby reflecting the efficiency of material utilization. According to the calculations, the W-I coupler design exhibits the highest MEF and is 3.59 to 9.77 times that of the other designs. In other words, the W-I-shaped coupler design can reduce core material usage by up to 87.7%. Consequently, this design has the highest core material utilization efficiency, which translates to the smallest size, the lightest weight, and the lowest cost for magnetic cores.

CHAPTER 4: PROTOTYPE DEVELOPMENT

4.0 Introduction

To test the system dynamically, a prototype has been developed, which includes both WPT and auxiliary equipment. The WPT comprises transmitters, transmitter inverter circuits, a receiver, a receiver rectifier circuit, and a control signal module. The auxiliary equipment consists of a movable platform, two tracks, a set of testing instruments, among other components. The prototype adopts the same coupler structure and topology as developed by Xu in references [9, 14].

Figure 4-1 illustrates the 3D model of the dynamic WPT system prototype.

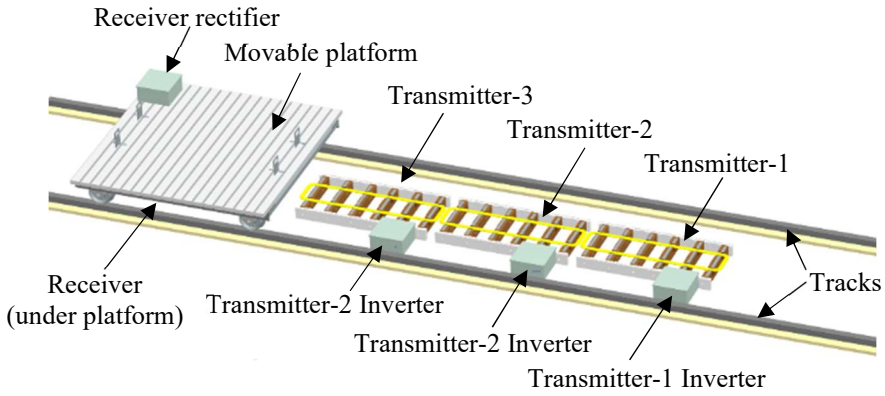

Figure 4-1: 3D model of dynamic WPT system prototype

In this system, there are three transmitters and one receiver. The receiver is suspended under the movable platform, with the receiver rectifier circuit placed on the platform. Three transmitters and their associated inverter circuits are situated between the tracks. The mobile platform is designed to move on the tracks autonomously and can carry a weight of more than 1,500 pounds.

The prototype's limitations include a maximum input voltage of 800 V DC and a total output power of 7.2 kW. Based on these limitations, a simulation model has been

used to calculate the maximum voltage and current values for each component, as detailed in Table 4-1.

Table 4-1: System component limitations

Parameter	Symbol	Value (Single)	Parameter	Symbol	Value (Single)
Input Power	P_{in}	7.2 kW	Output Power	P_{out}	7.0 kW
Input Voltage	V_{dc_in}	800 VDC	L_s Voltage	V_{Ls}	3057 V AC
Input Current	I_{dc_in}	9 A	L_s Current	I_{Ls}	20.5 A
L_R Voltage	V_{LR}	879 V AC	C_S Voltage	V_{CS}	3020 V AC
L_R Current	I_{LR}	8.9 A	C_S Current	I_{CS}	20.5 A
C_R Voltage	V_{CR}	691 V AC	C_{dc} Voltage	V_{Cdc}	297 V DC
C_R Current	I_{CR}	21.1 A	C_{dc} Current	I_{Cdc}	17.4 A
L_p Voltage	V_{Lp}	691 V AC	R_{dc} Voltage	V_{dc_out}	297 V DC
L_p Current	I_{Lp}	22.5 A	R_{dc} Current	I_{dc_out}	23.7 A
MOSFET Voltage	V_S	800 V DC	Diode Voltage	V_D	294 V DC
MOSFET Current	I_S	9 A	Diode Current	I_D	20.5 A

When designing and manufacturing the prototype, these limiting parameters will serve as the basis for selecting devices and determining constraints for the components. The remainder of this chapter will detail how each component is designed and verified.

4.1 Transmitter Side Components

4.1.1 System Topology and Key Components

The system topology, as depicted in Figure 4-2, consists of three transmitters (Tx1, Tx2, and Tx3) and one receiver (Rx). The transmitters, each incorporating a half LCL-S compensation topology, are connected in parallel to the same DC source.

Each transmitter in the system employs four C3M0021120D N-channel MOSFETs to generate a high-frequency AC at 85 kHz. All three transmitters are synchronized, using the same set of gate drive signals to generate AC concurrently. The parameters for these designed components are detailed in Table 4-2.

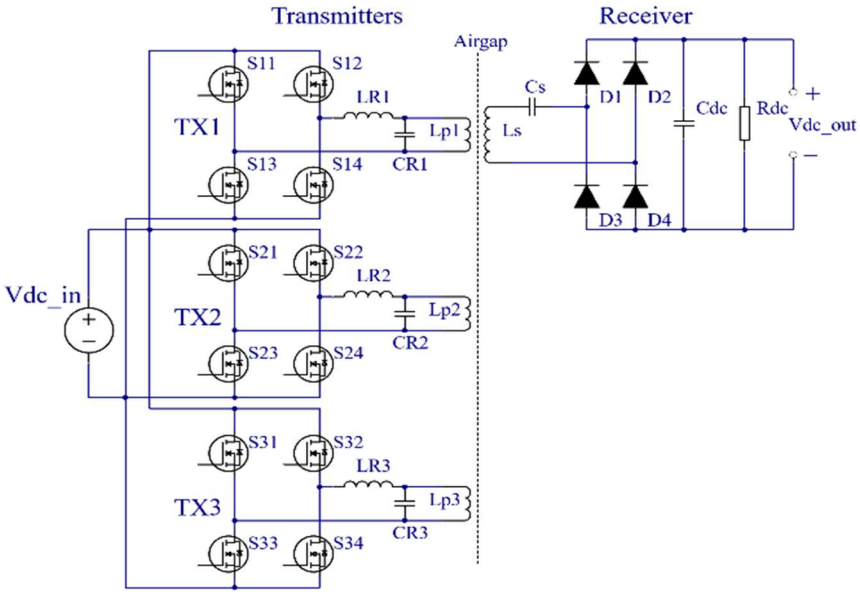

Figure 4-2: Three-transmitter and one-receiver LCL-S compensation topology

Table 4-2: Designed parameters of transmitter side components

Component	Symbol	Designed Value	Model
Tx Self-inductor	L_{p1}, L_{p2}, L_{p3}	71.70 uH	Handmade
Tx Resonant Inductor	L_{R1}, L_{R2}, L_{R3}	71.70 uH	Handmade
Tx Capacitor	C_{R1}, C_{R2}, C_{R3}	48.89 nF	B32656S2224J561 (9s2p configuration)
Inverter MOSFET	S11-S14, S21-S24, S31-S34	--	C3M0021120D

4.1.2 Transmitter Inverter Design

The inverter employs four C3M0021120D SiC Power N-channel MOSFETs. These chips have a drain-source voltage V_{DS} of 1200 V, a continuous drain current I_D of 81 A, and a drain-source on-state resistance $R_{DS(ON)}$ of 40 mΩ. Consequently, they are well-suited to meet the system's requirements, contributing to reduced power loss and cooling needs, and enhancing system efficiency and power density.

Ensuring the regular operation of the MOSFETs involves keeping the chip's temperature within the designed range. This requires calculating the chip's losses and

designing appropriate heat dissipation measures.

The losses in the chip mainly are from two sources: conduction losses and switching losses. Conduction losses occur when the MOSFET is in the ON state, relating to the voltage drop across the MOSFET during current conduction. Switching losses, which happen during the turn-on and turn-off stages, can be further divided into three components: gate loss (due to the total gate charge), output capacitor loss (due to the output capacitance C_{OSS}), and rise and fall loss (owing to rise time and fall time).

By setting the case temperature T_C to 75°C, the related parameters for calculating the switching losses are detailed in Table 4-3.

Table 4-3: Parameters of C3M0021120D MOSFET

Parameter	Symbol	Value
frequency	f	85000 Hz
Drain-Source Voltage	V_{DS}	800 V DC (Table 4-1: V_S)
Drain-Source Current	I_{DS}	9 A (Table 4-1: I_S)
Zero Gate Voltage Drain Current	I_{DSS}	50 uA
Duty Cycle	D_C	0.5
Gate Voltage	V_{GS}	15 V
Drain-Source On-State Resistance	$R_{DS(ON)}$	25 mΩ
Total Gate Charge	Q_g	160 nC
Output Capacitance	C_{oss}	180 pF
Rise Time	t_r	27 ns
Fall Time	t_f	25 ns

The power loss for each source can be calculated by the following equation:

Conduction Losses:

$$P_{CL} = D_C {I_{DS}}^2 R_{DS} = 1.0125\ W \tag{21}$$

Switching Losses:

$$P_{SW} = 0.5 V_{GS} Q_g f + 0.5 C_{OSS} V_{DS}^2 f + 0.5\left(t_r + t_f\right) V_{DS} I_{DSS} f = 5.0108\ W \tag{22}$$

The total loss for the inverter with four chips is 24.093 W. Based on the calculation result, the heat sink and cooling fan will be used for cooling the control system.

4.1.3 Transmitter Mechanical Structure

The mechanical structure of the transmitter (Tx), as depicted in Figure 4-3, comprises two side bars, six W-shaped cores, twelve coil holders, six cross bars, and the transmitter coils. The side bars and cross bars, which are connected by plastic fasteners, form the main frame of the structure. The W-shaped cores and coil holders are securely fixed into the notches of the cross bars. The coil holders are designed to support the coils.

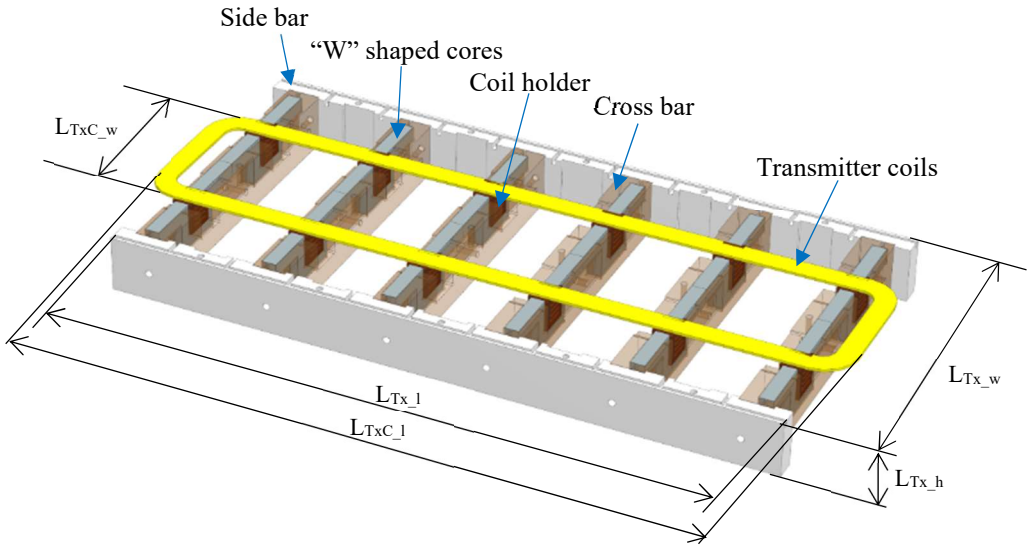

Figure 4-3: Transmitter mechanical structure

The mechanical dimensional parameters are depicted in Table 4-4.

Table 4-4: Transmitter mechanical dimensions

Parameter	Symbol	Value
Tx Frame Length	L_{Tx_l}	48 in / 121.9 cm
Tx Frame Width	L_{Tx_w}	24 in / 60.69 cm
Tx Frame Height	L_{Tx_h}	4 in / 10.16 cm
Tx Coils Length	L_{TxC_l}	49 in / 124.46 cm
Tx Coils Width	L_{TxC_w}	11 in / 27.94 cm

The mechanical dimensions of the W-shaped core are shown in Figure 4-4. Figure 4-4 (a) presents the front view, while Figure 4-4 (b) shows the side view.

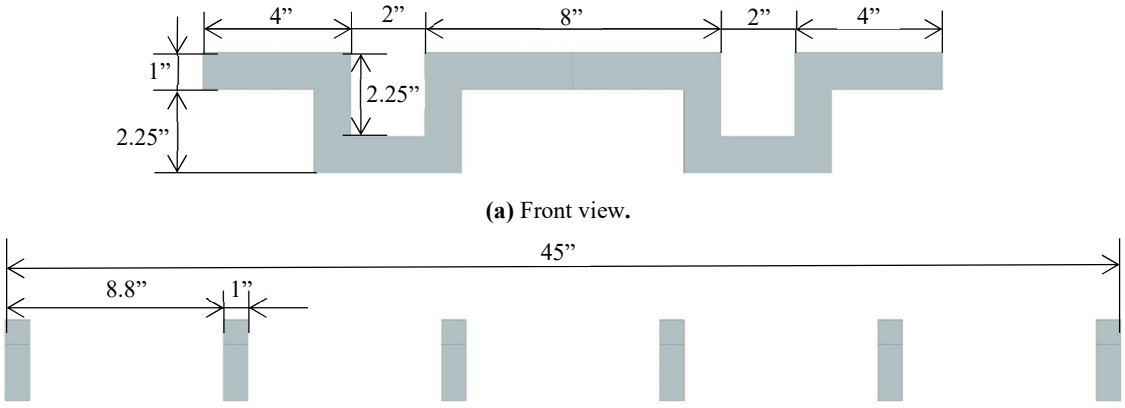

(a) Front view.

(b) Side view.

Figure 4-4: W-shaped core mechanical dimensions

4.1.4 Resonant Capacitors C_R

The transmitter resonant capacitors C_{R1}, C_{R2}, and C_{R3}, are composed of 18 capacitors (model: B32656S2224J561). They are arranged in a 9s2p configuration, with “9” capacitors connected in series and “2” capacitors connected in parallel, as depicted in Figure 4-5. And based on the calculations, the circuit parameter limitations for C_R are detailed in Table 4-5.

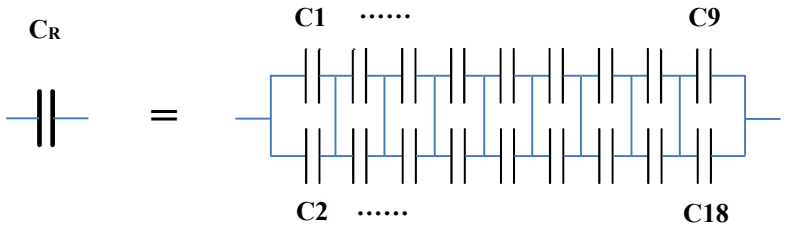

Figure 4-5: 9s2p configuration of C_R

Table 4-5: Component rating values and circuit limitations for C_R

Parameter	Symbol (for single)	Rating Value (for single)	Symbol (for C_R)	Rating Value (for C_R)	System Limitation
Permissible voltage @ 85kHz	V_{RMS}	93 V AC	$V_{RMS\text{-}CR}$	842 V AC	691 V AC (Table 4-1)
Permissible current @ 85kHz	I_{RMS}	11 A	$I_{RMS\text{-}CR}$	22 A	21.1 A (Table 4-1)
Capacitance	C	220 nF	C_R	48.89 nF	----

The measured capacitance values of C_{R1}, C_{R2}, and C_{R3}, are listed in Table 4-6. Due to the differences between calculated and actual values, they slightly deviate from the values presented in Table 4-2. When manufacturing inductors or coils, it is crucial to use these measured capacitance values to determine the inductance, ensuring that the system's resonant frequency remains at 85 kHz.

Table 4-6: Measured values of C_R

Location	Symbol	Measured Value
Tx1	C_{R1}	48.26 nF
Tx2	C_{R2}	48.94 nF
Tx3	C_{R3}	48.90 nF

4.1.5 Resonant Inductor L_R and Primary Coil L_p

Considering that the system functions under conditions of high frequency and high current, stranded Litz wire is selected for fabricating the inductors and coils. This choice helps to mitigate the skin effect and minimize conduction loss. The measured inductance values for the primary coils L_p and the resonant inductor L_R on the transmitter side are provided in Table 4-7.

Table 4-7: Measured values of transmitter inductors

Location	Symbol	Measured Value
Tx1	L_{R1}, L_{p1}	72.64 uH
Tx2	L_{R2}, L_{p2}	71.63 uH
Tx3	L_{R3}, L_{p3}	71.70 uH

4.1.6 Transmitter Control

The transmitters for the WPT system, primarily installed on outdoor tracks for railway applications, pose a significant safety challenge. When powered on, the transmitters generate high voltage, reaching up to thousands of volts, which presents a substantial safety threat to people or animals. Consequently, a fundamental control procedure for WPT systems equipped with multiple transmitters is to activate them only when a train is passing through. More specifically, only the transmitters located directly below the receiver are activated. This strategy includes pre-activating the transmitters ahead of the receiver and deactivating those behind it.

Another challenge concerns the timing of operation. Firstly, the system must determine the relative position between the transmitters and receivers at which the energy exchange should start or stop. Following this, the optimal timing for switching the transmitters on and off can be determined by integrating the train's operating speed and position.

Moreover, ensuring the continuity and stability of energy transmission is crucial. This means that energy transmission should not experience sudden interruptions or significant fluctuations, which would help minimize the impact on the WPT system and other electronic components. An essential aspect of this is the synchronization between adjacent transmitters, which includes aligning the magnetic flux direction, frequency, and levels. These requirements are incorporated into transmitter control by synchronizing the gate drive signals of the inverter.

4.2 Receiver Side Components

4.2.1 System Topology and Key Components

The topology of the receiver side is depicted in Figure 4-2. It includes a self-inductor Ls, an Rx capacitor C_S, an output capacitor C_{dc}, a rectifier (comprising D1 to D4), and a load resistor R_{dc}. The designed parameters for these components are presented in Table 4-8.

Table 4-8: Designed parameters of receiver side components

Component	Symbol	Designed Value	Model
Rx Self-inductor	L_s	175.30 uH	Handmade
Rx Capacitor	C_S	20 nF (Total)	104HC1102K2CM6 (5s configuration)
Rectifier	D1, D2, D3, D4	--	MSC50DC120HJ
Receiver Capacitor	C_{dc}	20 uF	B25632B1127K100
Load resistor	R_{dc}	5-50 Ω	63204A-1200-160 Electronic load

The receiver capacitor C_S consists of five individual capacitors connected in series. The rectifier (D1 to D4) is a full H-bridge module that integrates four diodes. The load resistor is adjustable and regulated by an electronic load.

4.2.2 Receiver Mechanical Structure

The mechanical structure of the receiver, as illustrated in Figure 4-6, includes two side bars, two end bars, twelve I-shaped cores, six cross bars, and the receiver coils. The side bars, cross bars, and end bars are interconnected using plastic screws. The I-shaped cores are inserted into the notches of the cross bars, and the coils are positioned beneath these cores. The dimensional parameters of the receiver's mechanical structure are detailed in Table 4-9.

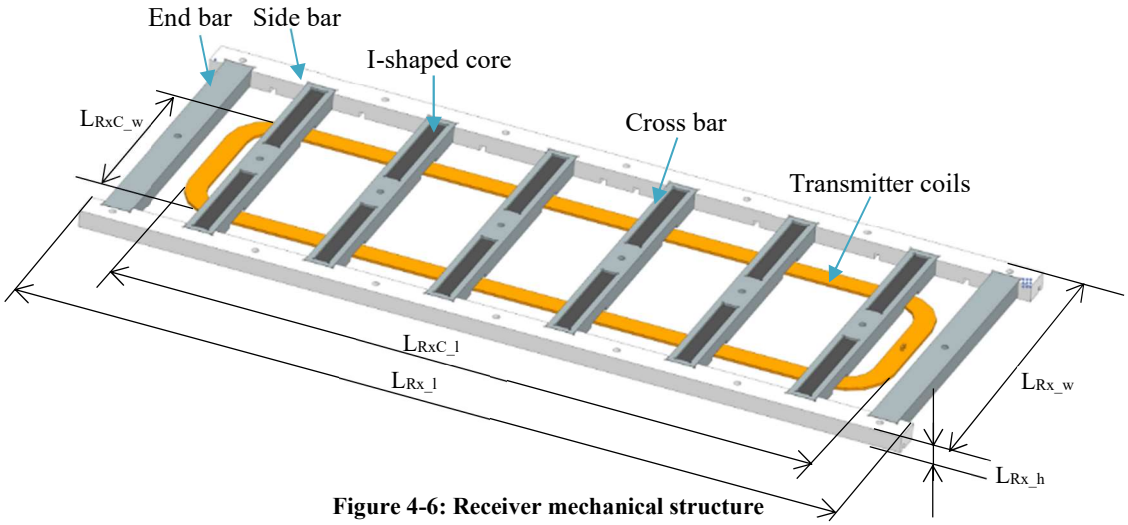

Figure 4-6: Receiver mechanical structure

Table 4-9: Receiver mechanical dimensions

Parameter	Symbol	Value
Rx Frame Length	L_{Rx_l}	60 in / 152.4 cm
Rx Frame Width	L_{Rx_w}	24 in / 60.69 cm
Rx Frame Height	L_{Rx_h}	1.25 in /3.175 cm
Rx Coils Length	L_{RxC_l}	52 in / 132.08 cm
Rx Coils Width	L_{RxC_w}	13.5 in / 34.29 cm

The mechanical dimensions of the I-shaped cores are shown in Figure 4-7. Figure 4-7 (a) is the front view, and (b) is the side view.

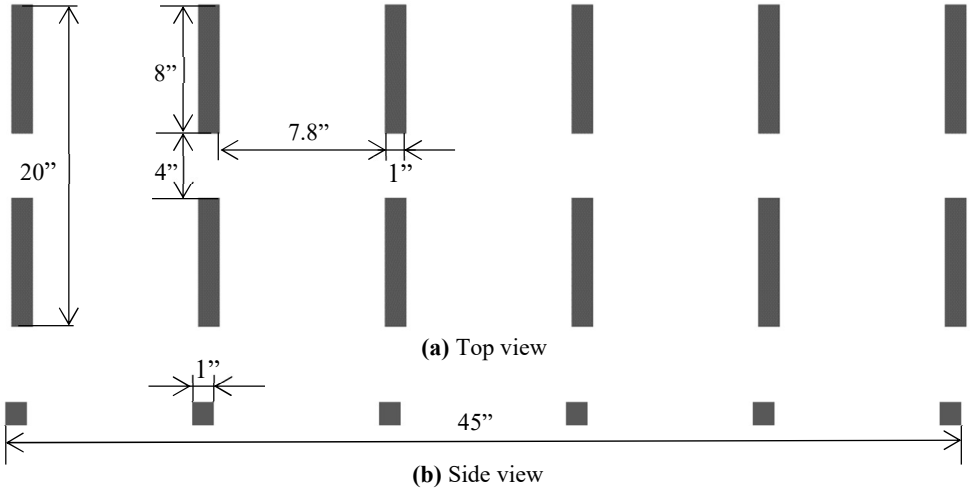

(a) Top view

(b) Side view

Figure 4-7: I-shaped core mechanical dimensions

4.2.3 Receiver Capacitor C_S

On the receiver side, the capacitor C_S is designed to have a capacitance of 20 nF. It is assembled using five 0.1 uF capacitors (104HC1102K2CM6), which are connected in series. Each individual capacitor can handle a maximum voltage of 1000 V and a maximum current of 65 A. Therefore, the combined C_S has a maximum voltage capacity of 5000 V and a current capacity of 65 A. According to the limitations outlined in Table 4-1, where the maximum voltage and current for C_S are specified as 3020 V and 20.5 A, respectively, this configuration is safe for use in the system. The measured capacitance of C_S is also confirmed to be 20 nF.

4.2.4 Receiver Self-inductor L_s

For the resonant WPT system, it is crucial that the transmitter and receiver have the same resonant frequency. To achieve a resonant frequency of 85 kHz with the 20 nF receiver capacitor C_S, the inductance of the receiver self-inductor L_s is set at 175.30 uH. Additionally, 1500/38 Litz wire is used to manufacture the coils, ensuring excellent high-frequency performance.

4.2.5 Receiver Rectifier

On the receiver side, an SiC diode full-bridge power module (MSC50DC120HJ, D1 to D4) is utilized to rectify AC back to DC. This module's low on-resistance and low forward voltage features will enhance the system with improved power density and efficiency.

4.3 Mutual Inductance and Coupling Factor

The mutual inductances between the receiver and the transmitters were measured, as shown in Table 4-10. Three mutual inductances, 26.46 uH, 26.51 uH, and 26.47 uH,

correspond to the receiver being completely aligned with the three transmitters. The three coupling factors can be calculated using the formula $k = \frac{M}{\sqrt{L_s L_p}}$, where k is the coupling factor, M is the mutual inductance, L_s is the self-inductance of the receiver, and L_p is the self-inductance of the transmitter. The calculated coupling factors for the receiver with the three transmitters are 0.235356, 0.235818, and 0.235330, respectively.

Table 4-10: Mutual inductance and coupling factor *k*

	Individual Inductance			Mutual Inductance		
Component	Symbol	Designed	Measured	Symbol	Measured	coupling factor k
Rx Self-inductor	L_s	175.30 uH	176.43 uH	--	--	--
Tx Self-inductor	L_{p1}	71.70 uH	72.64 uH	$M_{s\text{-}p1}$	26.46 uH	0.235356
	L_{p2}	71.70 uH	71.63 uH	$M_{s\text{-}p2}$	26.51 uH	0.235818
	L_{p3}	71.70 uH	71.71 uH	$M_{s\text{-}p3}$	26.47 uH	0.235330

4.4 Auxiliary Equipment

4.4.1 Movable Platform

The movable platform, as illustrated in Figure 4-8, features four wheels, a metal frame, and a wood panel. It is designed to handle loads of up to 1500 pounds.

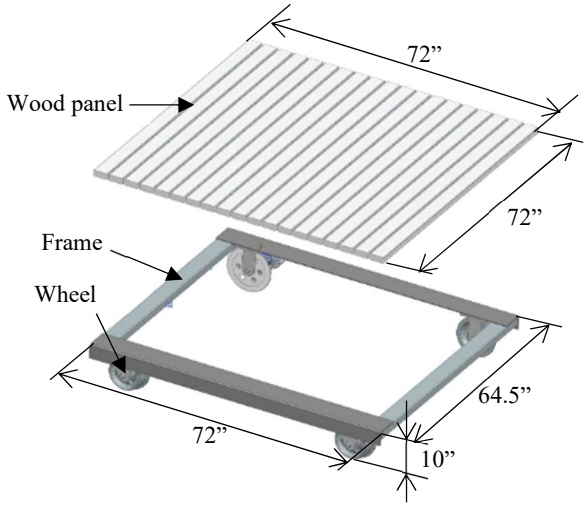

Figure 4-8: 3D model of movable platform

4.4.2 Tracks

The tracks are constructed using steel tubes and wood poles. The distance between the inner sides of the tracks is 56.5 inches, and their total length measures 432 inches. The detailed construction of the tracks is depicted in Figure 4-9.

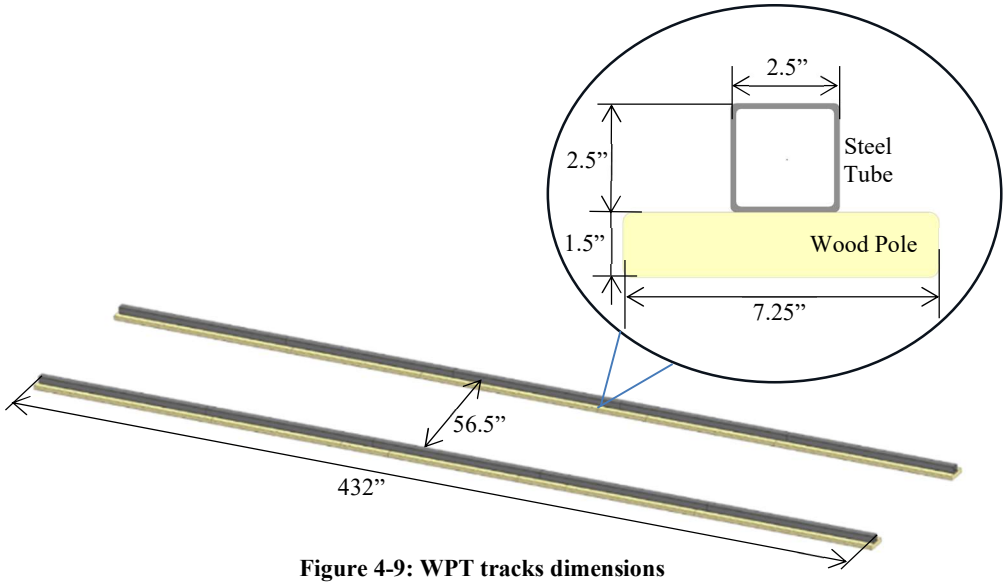

Figure 4-9: WPT tracks dimensions

4.5 Overlook of the Prototype

The prototype, as shown in Figure 4-10, features a movable platform and tracks. The receiver is suspended under the movable platform panel, and the three transmitters are positioned between the tracks. A DC source, with a voltage range of 0 to 1,000 volts, powers the transmitters. The transmitter inverters then convert this DC power to AC at a frequency of 85 kHz, enabling the transmitters to wirelessly transfer power to the receiver. The receiver rectifies the received AC voltage back to DC, which is then output to a DC electronic load.

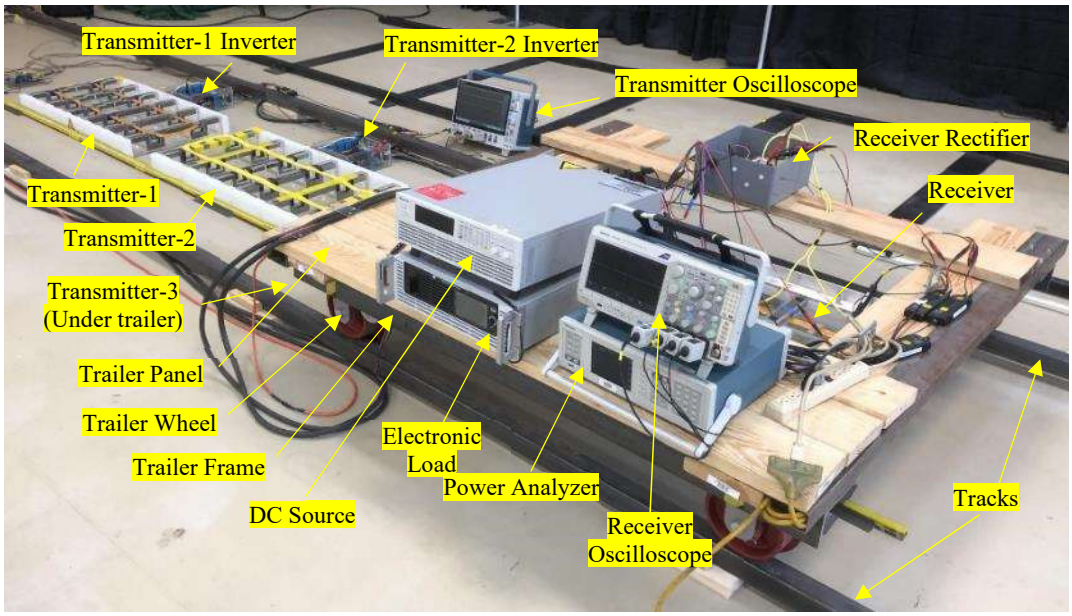

Figure 4-10: Prototype of the dynamic WPT system

The parameters of the prototype are shown in Table 4-11.

Table 4-11: Parameters of prototype

Component	Symbol	Designed	Measured Value
Tx Self-inductor	L_{p1}	71.70 uH	72.64 uH
	L_{p2}	71.70 uH	71.63 uH
	L_{p3}	71.70 uH	71.71 uH
Tx Resonant Inductor	L_{R1}	71.70 uH	72.64 uH
	L_{R2}	71.70 uH	71.63 uH
	L_{R3}	71.70 uH	71.71 uH
Tx Capacitor	C_{R1}	48.89 nF	48.26 nF
	C_{R2}	48.89 nF	48.94 nF
	C_{R3}	48.89 nF	48.90 nF
Rx Self-inductor	L_s	175.30 uH	176.43 uH
Rx Capacitor	C_S	20 nF	20 nF
DC Capacitor	C_{dc}	120 uF	120 uF
Load resistor	R_{dc}	5-50 Ω	5-50 Ω
Airgap	D_A	5 inches	5 inches
Frequency	f	85 kHz	85 kHz

CHAPTER 5: STATIC AND DYNAMIC ANALYSIS

5.0 Introduction

This chapter discusses experimental methods and the analysis of results, encompassing both static and dynamic experiments. In the static experiments, tests are conducted to identify the maximum efficiency point, determine the system's maximum efficiency, and measure the EMF values. In the dynamic experiments, the system's real-time output characteristics and efficiency are assessed.

5.1 Static Experiments

5.1.1 Experimental Setup and Waveforms

During the static experiments, a STSR setup, consisting of the receiver and transmitter-1, was utilized to verify the system's performance. This setup was powered by Chroma 62100H-1000, the load R_{dc} was simulated using Chroma 63200A electronic load, and the system's efficiency was measured with Tektronix PA3000 power analyzer. These components are depicted in Figure 5-1. The input power was measured before the inverter, while the output power was gauged after the DC capacitor C_{dc}.

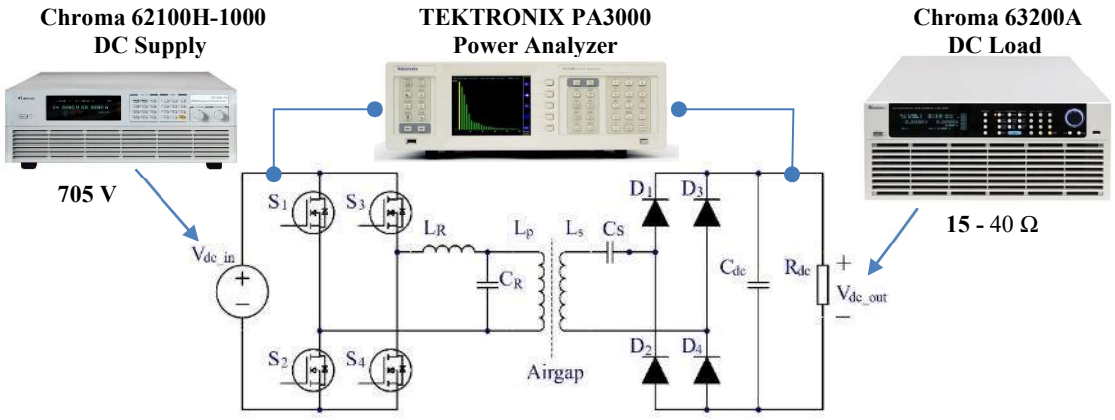

Figure 5-1: Experimental setup for static STSR

Figure 5-2 shows the experimental setup and waveforms of the STSR model with a load resistor R_{dc} of 10 Ω.

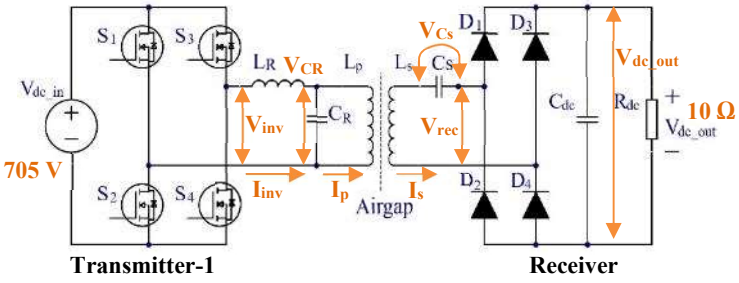

(a) STSR diagram and measurement check points

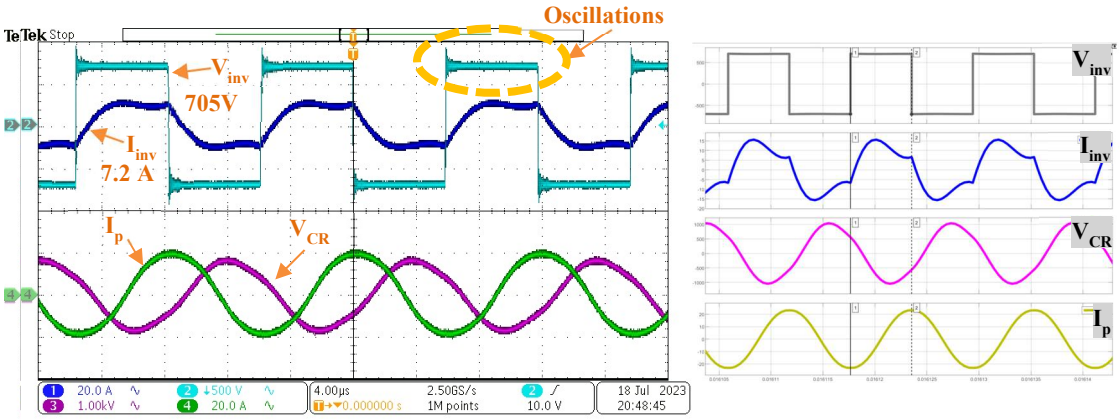

(b) Transmitter side measured and simulated waveforms

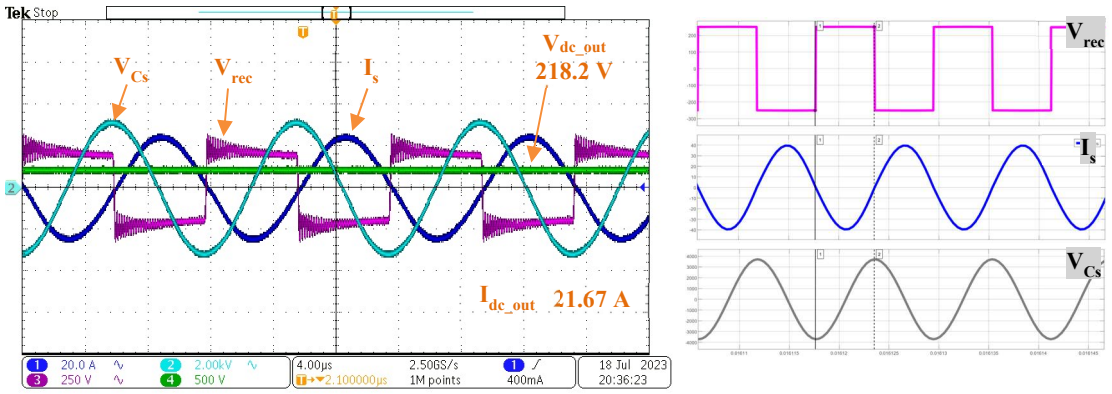

(c) Receiver side measured and simulated waveforms

Figure 5-2: Experimental waveforms for static STSR

Figure 5-2 (a) illustrates the diagram and the location of each measurement taken during the experiment. These include the output voltage V_{inv} and current I_{inv} of the inverter; the voltage V_{CR} on the resonant capacitor C_R; the current I_p in the primary coils L_p; the

current I_s in the secondary coils L_s; the voltage V_{Cs} on the receiver capacitor C_s; the voltage V_{rec} before the rectifier; and the output voltage V_{dc_out} of the receiver. Figure 5-2 (b) presents the measured and simulated waveforms on the transmitter side, while Figure 5-2 (c) displays those on the receiver side.

Comparing the measured results with the simulation, similar waveforms are observed. However, some differences are evident. In Figure 5-2 (b), the experimental results show notable oscillations in the waveform of V_{inv}, and a similar phenomenon is observed in the V_{rec} waveform on the receiver side in Figure 5-2 (c). These oscillations, characteristic of LC circuits, are likely due to the presence of parasitic inductance, capacitance, and resistance within the circuit. They cause the circuit's peak voltage to increase, which poses insulation challenges to components and conductors and contributes to increased circuit losses. While complete elimination of LC circuit oscillation is impractical due to inevitable parasitic elements and circuit impedance, mitigation is possible through circuit optimization and other methods.

5.1.2 Maximum Efficiency of STSR

The maximum efficiency η_{max} is a crucial parameter indicative of the system's performance. To determine η_{max}, a two-step test was conducted. The first step involved testing the system with a constant input voltage across various load resistors R_{dc} to identify the resistor at maximum efficiency R_{ME}. The second step entailed testing the system with different input voltages at R_{ME} to find η_{max} and the corresponding input and output power voltages.

For the first-step test, the input voltage was set to 650 V DC for transmitter-3 (Tx3), and the load resistors R_{dc} were varied from 10.0 to 40.0 Ω. The results, as shown in Figure

5-3, reveal that the maximum DC-to-DC efficiency of 93.40% is achieved at an R_{dc} of 21 Ω, with an input power of 2437 W and an output power of 2276 W.

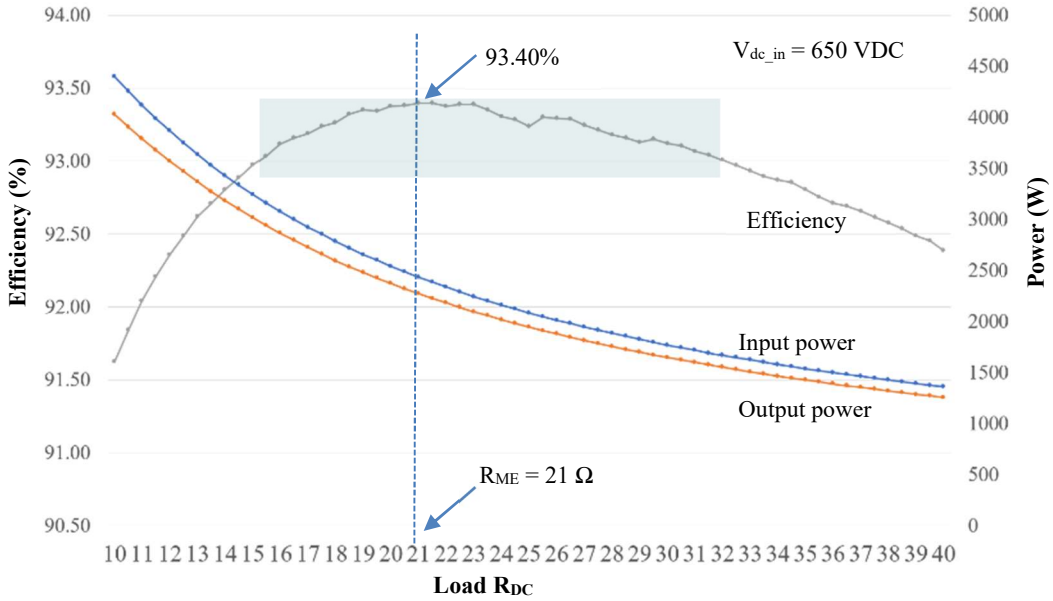

Figure 5-3: Efficiency at different R_{dc} (Tx3)

For the second step, the load resistor was fixed at R_{ME}, which is 21 Ω, and the input voltage gradually increased from 200 to 750 V DC. The results, as illustrated in Figure 5-4, show that the maximum DC-to-DC efficiency of 93.61% is attained at the highest input voltage of 750 VDC. At this voltage, the system has an input power of 3442 W and an output power of 3222 W.

After determining the maximum efficiency of transmitter Tx3, the other two transmitters were also tested. Subsequently, the maximum efficiency of the entire system was evaluated. Ultimately, the highest DC-DC efficiency η_{max} of 94.73% was achieved for Tx1, with input and output voltages of 727.05 V and 251.44 V, respectively. The corresponding input and output powers were 3168 W and 3001 W.

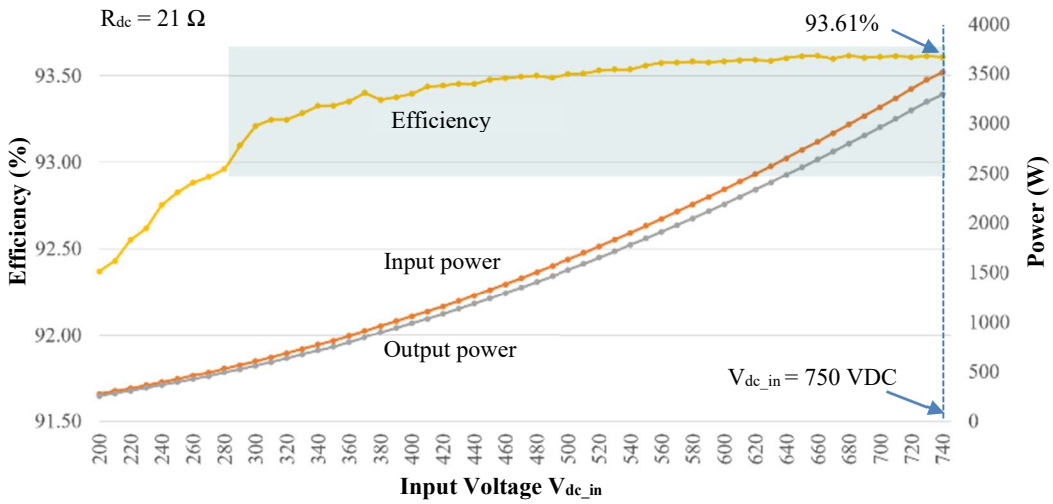

Figure 5-4: Efficiency at different input voltage (Tx3)

Furthermore, it was observed that the system maintains a broad range of high DC-DC efficiency. For instance, an efficiency of over 93% was achieved with the load resistor R_{dc} ranging from 15 to 32 Ω, as shown in Figure 5-3, and with input voltage varying from 280 to 750 VDC, as depicted in Figure 5-4. This characteristic provides the system with significant adaptability to different power sources and load conditions.

At the maximum efficiency point, the efficiencies of each system section were also evaluated, as illustrated in Figure 5-5. The measured values of $\eta_{DC\text{-}DC}$ and $\eta_{AC\text{-}AC}$ are 94.73% and 98.13%, respectively. The calculated values for $\eta_{inverter}$ and $\eta_{rectifier}$ are 97.75% and 98.76%, respectively. Here, $\eta_{inverter}$ indicates the efficiency of the inverter, $\eta_{AC\text{-}AC}$ represents the efficiency between the output of the inverter and the input of the rectifier, $\eta_{rectifier}$ suggests the efficiency of the rectifier, and $\eta_{DC\text{-}DC}$ denotes the efficiency between the input of the inverter and the output of the rectifier.

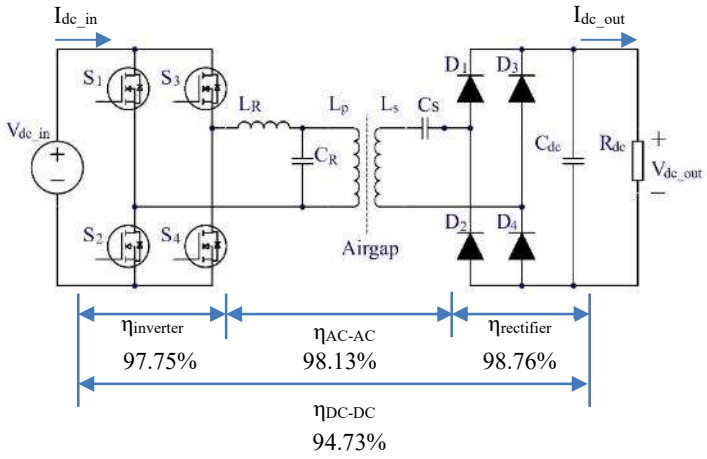

Figure 5-5: Efficiencies along the transmission path of STSR

To identify the system performance, more experiments were performed at a range of load resistors R_{dc} from 15.5 to 34 Ω, and a range of input V_{dc_in} from 100 to 500 V DC, and the efficiency map corresponds to R_{dc} and V_{dc_in} are shown in Figure 5-6.

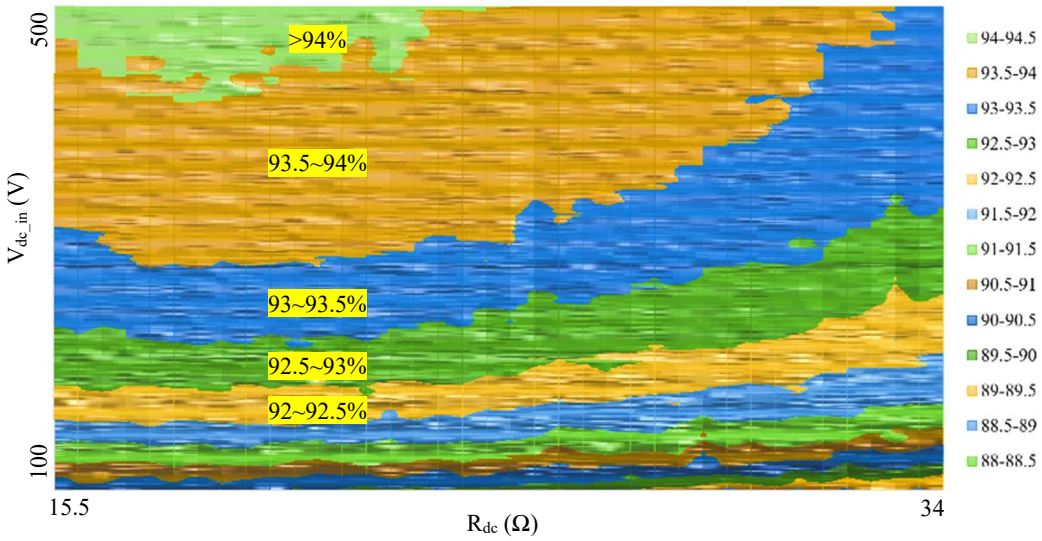

Figure 5-6: Efficiency map on various R_{dc} and various V_{dc_in}

From the data presented in the figure, it is evident that within the tested range of load resistors, the system tends to achieve high efficiency, particularly between 16 and 25 Ω. Additionally, from the perspective of input voltage, the system's efficiency improves with increasing voltage. Moreover, the system can get high efficiency in a big range of

input voltage and load resistor. These test results offer valuable insights and references for the system's future applications.

5.1.3 Efficiency vs. Misalignment of STSR

To analyze the impact of misalignment on the system's efficiency, the efficiency versus misalignment test was conducted for the STSR setup at the point of maximum efficiency, with the load resistor R_{dc} set to 21 Ω.

The test setup, as illustrated in Figure 5-7, included the following parameters: an input voltage V_{dc_in} of 705V, a frequency f of 85 kHz, a load resistor R_{dc} of 21 Ω, an air gap of 5 inches, and a maximum output power of 3000 W. The receiver was moved above the transmitter from a misalignment distance D_{mis} of -52 inches to +52 inches. This movement means that the receiver starts 52 inches away (Position A), passes directly over the transmitter (Position B, where D_{mis} is 0), and continues to a point 52 inches on the other side (Position C).

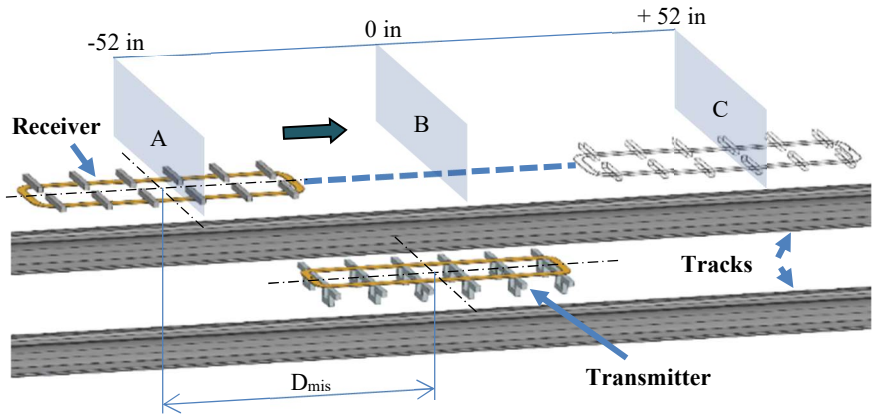

Figure 5-7: Misalignment experimental setup of STSR

During the test, it was observed that there was no output DC voltage when the receiver coils and transmitter coils were completely misaligned, that was, when the misalignment distance D_{mis} exceeded 48 inches. The receiver began to produce an output

voltage when the misalignment distance was within 48 inches. As the receiver approached the transmitter, the output voltage increased, reaching its maximum value when the two coils were aligned (D_{mis} is 0). Conversely, as the receiver moved away from the transmitter, the output decreased. The output voltage dropped to zero when the misalignment distance exceeded 48 inches.

The test results for the input current I_{dc_in}, output voltage V_{dc_out}, and output current I_{dc_out} versus the misalignment distance D_{mis} are presented in Figure 5-8. The figure features three curves: the upper curve represents the output voltage V_{dc_out}, the middle curve represents the output current I_{dc_out}, and the lower curve represents the input current I_{dc_in}. Throughout the test, the input voltage remained a constant DC of 705 V, and the load resistor was set to 21 Ω.

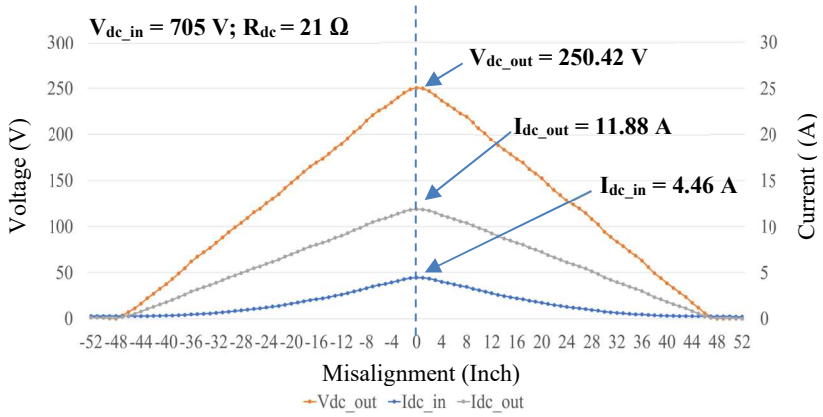

Figure 5-8: Current and voltage vs. misalignment (Tx1)

The output voltage and current waveforms resemble triangles. The relationship between the output voltage and misalignment during the rising and falling stages appears to be relatively linear. According to (4), $V_{dc\_out} = V_{dc\_in}\omega^2 M C_R = V_{dc\_in} M \frac{1}{L_R}$, the output voltage V_{dc_out} is only related to the input voltage V_{dc_in}, the mutual inductance M and the

transmitter resonant inductance L_R. When V_{dc_in}, and L_R are fixed, the output voltage is only linearly related to the mutual inductance M. Accompanied by a constant load resistance R_{dc}, the output current I_{dc_out} is also linear.

The input current exhibits a parabolic shape, resulting from the constant input voltage and an electronic load in constant resistance mode. According to the formulation, $I_{dc_{in}} = \frac{V_{dc\_out}^2}{R_{dc}V_{dc\_in}}$, when V_{dc_out} increases linearly, the input current I_{dc_in} assumes a parabolic profile.

The experiment results indicate that the maximum V_{dc_out} is 250.42 V, the maximum I_{dc_out} is 11.88 A, and the maximum I_{dc_in} is 4.46 A. The mutual inductance and coupling factor under these test conditions are calculated to be 25.80 uH and 0.227920, respectively. Compared with the measured values in Table 4-10, which are 26.46 uH and 0.235356, there is a discrepancy of about 2.56%, attributable to the specific test conditions.

Another crucial parameter is the DC-DC efficiency $\eta_{DC\text{-}DC}$, which measures the efficiency from DC input to DC output. Figure 5-9 presents the waveforms of the input power P_{dc_in}, output power P_{dc_out}, and DC-DC efficiency $\eta_{DC\text{-}DC}$ versus misalignment. The experiment results show that the maximum input power is 3102.26 W, the maximum output power is 2938.69 W, and the DC-DC efficiency reaches up to 94.73%. The efficiency curve also demonstrates excellent anti-misalignment performance; for instance, the system efficiency still exceeds 85% at a misalignment of 28 inches. Therefore, from an energy-saving perspective, the system holds significant practical value.

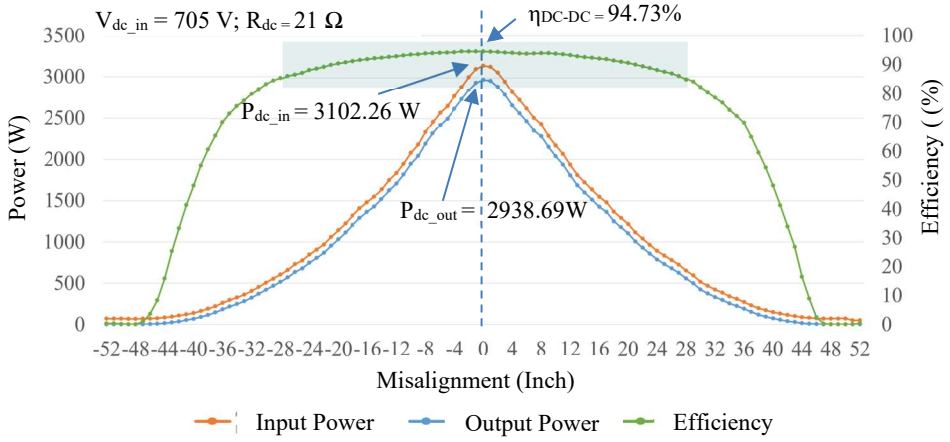

Figure 5-9: Power and efficiency vs. misalignment (Tx1)

Additionally, it is evident from the figure that the system's input and output powers are highly sensitive to misalignment. These power levels decrease rapidly as the misalignment increases. Therefore, maintaining proper alignment is essential for achieving high-power transmission in the system.

5.2 Dynamic Experiments

5.2.1 Experimental Setup

The dynamic experiments were conducted using an MTSR model, which comprised three transmitters and one receiver. The test setup was as follows: The input power was set at 3 kW with an input DC voltage of 500 V and a load resistor of 15 Ω. The distance between the coils of the two transmitters (D_{TT}) was 0 inch, and the air gap between the receiver and transmitter was set at 5 inches. The receiver moved from -30 inches relative to transmitter-1 at a speed of 15 feet per second, continuing past transmitter-3 by 30 inches. This means the distance between the center of the receiver and the center of transmitter-2 ranged from -130.5 inches (to the left) to +130.5 inches (to the right). Figure 5-10 illustrates the experimental setup, showing only the coils and cores, with the frames and other

components omitted for clarity.

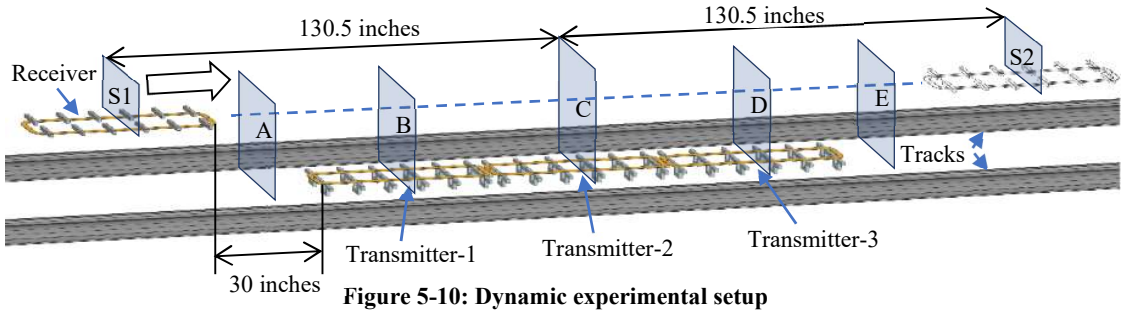

Figure 5-10: Dynamic experimental setup

As illustrated in the figure, there are seven critical positions: S1, S2, and from A to E. Position S1 is the starting point, while S2 marks the ending position. Position A is where the transmitter begins to output power, B is where the receiver aligns with transmitter-1, C marks the alignment of the receiver with transmitter-2, D is the point of alignment with transmitter-3, and E is where the receiver's output drops to zero. During the dynamic experiment, the receiver moves from position S1 to S2, sequentially passing through points A, B, C, D, and E.

5.2.2 Experimental Results and Analysis

The experimental results are reported in Figure 5-11. Figure 5-11 (a) displays the parameters of the experimental circuit. On the transmitter side, I_{Tx1} represents the input current of transmitter-1, I_{Tx2} corresponds to the input current of transmitter-2, and I_{Tx3} denotes the input current of transmitter-3. Additionally, I_{Total} represents the total input current of the three transmitters.

Figure 5-11 (b) presents the experimental results, which are divided into five sections: The voltage section displays the input voltage V_{dc_in} and the output voltage V_{dc_out}; The current section illustrates the current values for each transmitter, namely, I_{Tx1}, I_{Tx2}, I_{Tx3}, the total input current I_{Total}, and the output current I_{dc_out}; The power section showcases the

input power P_{in} and the output power P_{out}; The efficiency section demonstrates the efficiency observed during the test; The misalignment section provides information on the location of the receiver.

The system characteristics at different locations are described as follows:

Position S1: During the experiment, the receiver is initially positioned at S1, which corresponds to -130.5 inches between the middle of the receiver and the middle of transmitter-2. No power was transferred at this point due to the significant distance between the receiver and transmitter. However, there was still some input power, approximately 230 W, due to circuit losses.

Position A: When the receiver moved to position A, the receiver coils began to align with the Tx1 coils, corresponding to -98 inches. At this point, a current was induced in the receiver coils, causing I_{Tx1} on the transmitter side to increase. Consequently, the system started to output voltage, current, and power, and the efficiency was no longer zero.

From A to B: As the receiver continued to approach the transmitter, more sections of the receiver coils aligned with the Tx1 coils. This alignment resulted in a significant increase in the current within the receiver coil, with the rate of increase being proportional to the receiver's speed. Simultaneously, the system's output voltage, current, power, and efficiency all increased.

Position B: Upon reaching position B, the receiver coils aligned perfectly with the Tx1 coils, corresponding to -50 inches. At this juncture, I_{Tx1} reached its peak value, and the receiver coils generated the maximum current. The system operated at its maximum output voltage, current, power, and efficiency. At this moment, I_{Tx2} began to increase as the receiver coils were very close to the Tx2 coils.

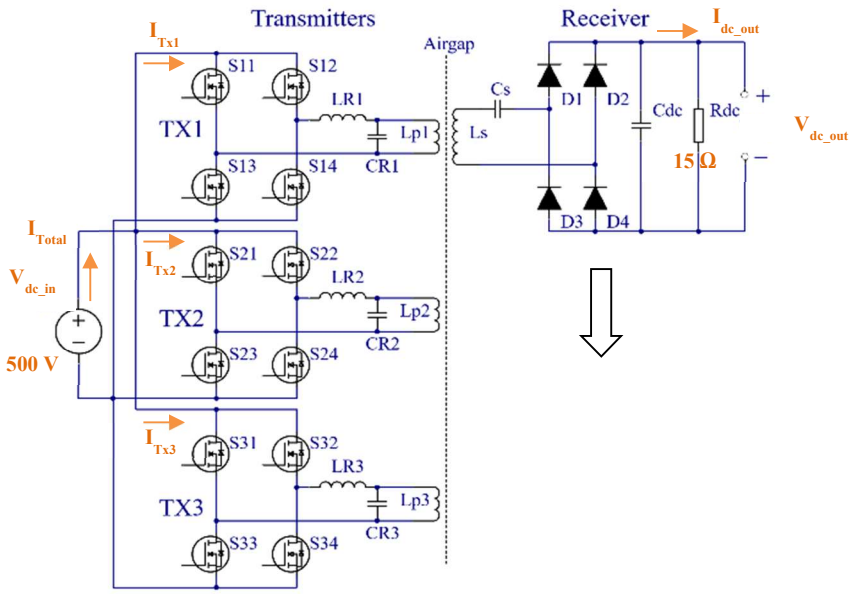

(a) Experimental parameters

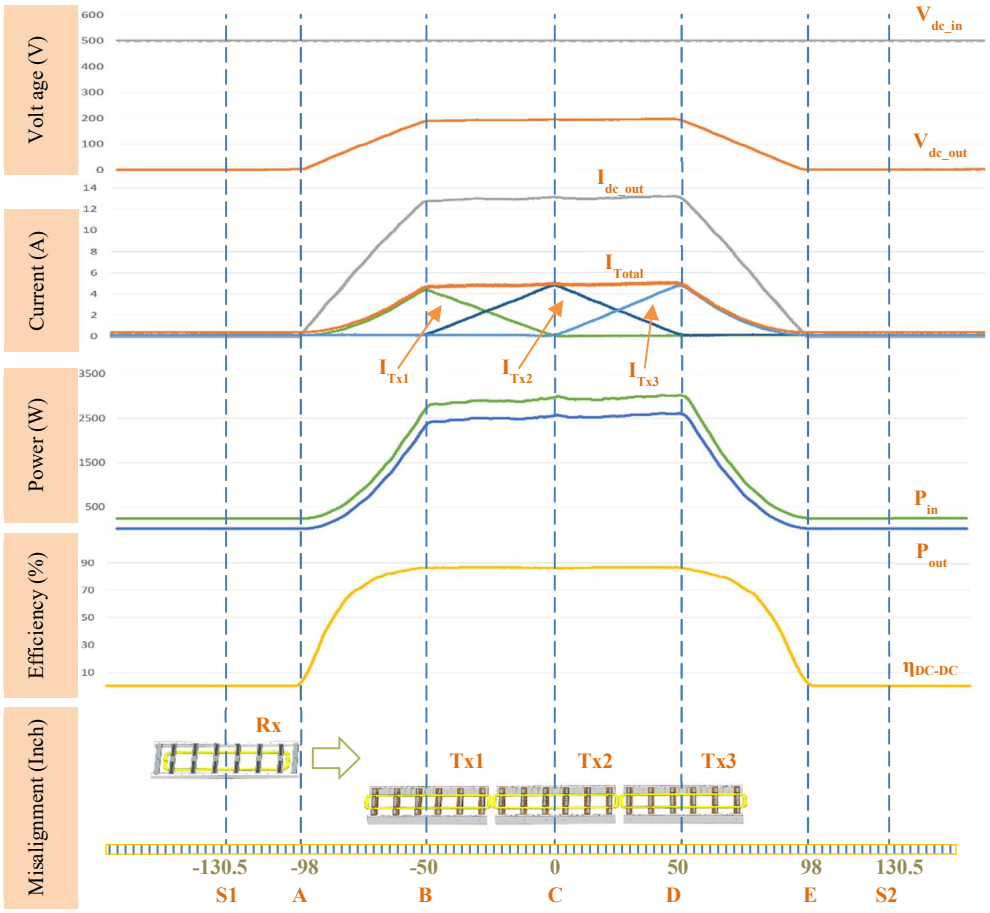

(b) Experimental results

Figure 5-11: Dynamic experimental setup and results

From position B to C: As the receiver moved away from transmitter-1 and approached transmitter-2, the receiver coils began to align with both the Tx1 and Tx2 coils simultaneously. The area of coupling with Tx1 decreased, while the area of coupling with Tx2 increased. Consequently, I_{Tx1} decreased, I_{Tx2} increased, and Tx2 started transmitting more energy. The result was a stable output, and the system maintained maximum power output and efficiency.

Position C: When the receiver reached position C, the receiver coils aligned perfectly with the Tx2 coils, corresponding to 0 inches. At this point, I_{Tx2} reached its peak value, I_{Tx1} reduced to almost 0, and I_{Tx3} increased as the receiver coils aligned with Tx3. The system remained stable, operating at maximum power output and efficiency.

From C to E: Like the earlier transition from A to C, the output characteristics from C to E followed a symmetric pattern. As the receiver moved away from Tx2, aligned with Tx3, and eventually moved away from Tx3, the input current gradually shifted from Tx2 to Tx3, eventually decreasing to zero. The system's output power and efficiency also decreased from their maximum values to zero.

From E to S2: During this phase, the system had no output.

It's worth noting that in Figure 5-11 (b), a slight upward trend in the output voltage and current can be observed during the system's stable output phase. This indicates that the system's output is not entirely stable. This behavior is attributed to the slightly inferior performance of transmitter-1 compared to transmitter-2 and transmitter-3. To address this issue, circuit optimization may be necessary.

Additionally, it should be mentioned that due to the experiment not selecting the maximum efficiency point and considering the circuit losses between the transmitters, the

system's maximum efficiency was only approximately 89%.

5.2.3 Analysis of Power and Input Equivalent Series Resistance (ESR_{in})

The system's power loss can be calculated by $P_{loss} = P_{in} - P_{out}$, and the curve is shown in Figure 5-12. The trend in power loss resembles that of both input and output power. The P_{loss} starts to increase when the receiver is at position A, and it gets the maximum value when the receiver aligns with Tx1 to Tx3, from position B to C. After passing position D, the P_{loss} starts to decrease and reduces to 0 at position E. This is comprehensible since an increase in current within the circuit leads to a proportional rise in losses.

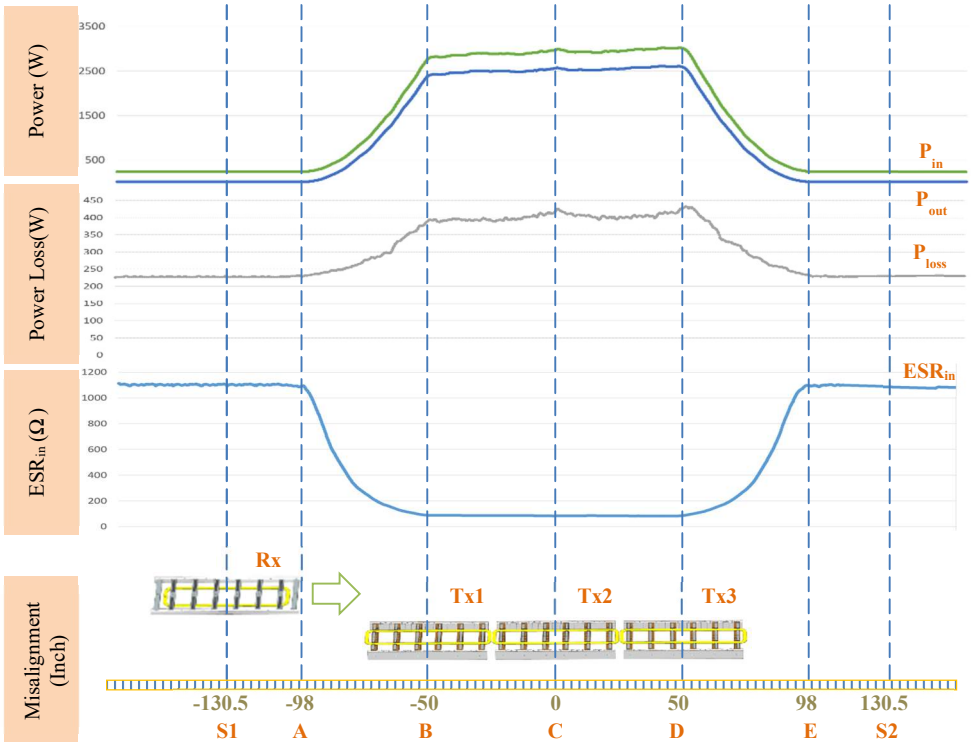

Figure 5-12: Dynamic analysis of power and ESR

The input ESR_{in} can be calculated by the formulator, $ESR_{in}=P_{in}/I^2_{Total}$, also plotted in Figure 5-12. The ESR_{in} drops significantly when the receiver is close to the transmitter, and then stays at a very low value when the receiver aligns with the transmitters. This also shows from another perspective why the system can transmit more considerable power and

maintain higher efficiency when the receiver aligns with transmitters.

5.2.4 Analysis of Performance

Based on the experimental results, it is observed that the system's input and output power increase smoothly from zero to their maximum values as the receiver approaches the transmitter. Similarly, as the receiver moves away from the transmitter, both input and output power decrease smoothly back to zero. These characteristics are advantageous for practical applications, as they help mitigate the impact of excessive dv/dt and di/dt on the system and the power grid. Additionally, when the receiver is positioned above the transmitters, the system's input and output power are maintained at their maximum values with high stability during the switching process between two transmitters. This stability is beneficial for ensuring consistent output in real-world applications. Moreover, the system can maintain its highest efficiency at (n-1)/n of the transmitter's total length. This capability is advantageous for addressing misalignment issues in static charging and for improving overall efficiency in dynamic charging.

5.3 EMF Analysis

5.3.1 EMF Standards and Measurement Methods

The International Commission on Non-Ionizing Radiation Protection (ICNIRP) has developed guidelines to limit exposure to electric and magnetic fields (EMF) and protect against all known adverse health effects. These guidelines cover the low-frequency range from 1 Hz to 100 kHz. Initially, the ICNIRP 1998 guidelines [57] were introduced, which were later superseded by the ICNIRP 2010 guidelines [58].

According to the ICNIRP 2010, there are two categories of reference levels: Occupational Exposure and General Public Exposure. The specific values for these

reference levels are detailed in Table 5-1.

Table 5-1: ICNIRP 2010 reference levels for magnetic flux density B

Occupational Exposure		General Public Exposure	
Frequency Range (Hz)	Magnetic Flux Density B (T)	Frequency Range (Hz)	Magnetic Flux Density B (T)
1 Hz-8 Hz	$0.2 / f^2$	1 Hz-8 Hz	$4\times10^{-2} / f^2$
8 Hz-25 Hz	$2.5\times10^{-2} / f$	8 Hz-25 Hz	$5\times10^{-3} / f$
25 Hz-300 Hz	1×10^{-3}	25 Hz-50 Hz	2×10^{-4}
--	--	50 Hz-400 Hz	2×10^{-4}
300 Hz-3 kHz	$0.3 / f$	400 Hz-3 kHz	$8\times10^{-2} / f$
3 kHz-10 MHz	1×10^{-4}	3 kHz-10 MHz	2.7×10^{-5}

Notes: f – the frequency of magnetic fields, unit in Hz

The frequency of the WPT system is 85 kHz, which is in the range of 3 kHz - 10 MHz. Therefore, the reference levels for Occupational Exposure and General Public Exposure are 1×10^{-4} Tesla (100 uT), and 2.7×10^{-5} Tesla (27 uT), respectfully.

EMF measurements are conducted to assess the electromagnetic impact of a WPT system on its surroundings, particularly to determine the potential electromagnetic interferences that could affect human health. Lin, in [52], provides a comprehensive description of the significance, standards, and methods for EMF measurement in WPT systems. Additionally, Lin developed a WPT model based on finite element analysis (FEA) and designed and tested methods to mitigate the system's EMF emissions.

On the transmitter side, the primary focus is measuring the EMF strength in areas accessible to people around the transmitters under two conditions: the unloaded state and the 3 kW power output state. In the unloaded state, the transmitters are powered on, but no receivers are placed directly above them. In the 3 kW power output state, the receivers are positioned above the transmitters and are actively transmitting power.

On the receiver side, the measurements include the electromagnetic field strength at various positions above the receiver. These measurements serve as reference points for

analyzing the EMF at the train's floor level.

5.3.2 Static EMF Measurements

The measurements involve multiple cross-sections of two transmitters, as depicted in Figure 5-13. The designated positions are as follows: Position A at the front end of Transmitter-2, Position B at the middle of Transmitter-2, Position C at the rear end of Transmitter-2 (which is also the front end of Transmitter-3), Position D at the middle of Transmitter-3, and Position E at the back end of Transmitter-3. Data collection occurs as the Electromagnetic Meter (EM) moves from left to right above the ground at a height of 7.5 inches (which is 3.5 inches above the transmitter coils).

The curves representing the five cross-sections illustrate the EMF measurements relative to the physical locations of the EM. By linking points with identical EMF values at various locations, an EMF contour map can be generated. This map highlights the ICNIRP 2010 reference levels for Occupational Exposure and General Public Exposure, set at 100 *u*T and 27 *u*T, respectively. According to this map, the area with EMF values exceeding 100 uT is primarily confined within the transmitter's frame. Conversely, the region where the EMF ranges from 27 to 100 uT extends no more than 7 inches outward from the transmitter's frame. Importantly, in the areas beyond the tracks, where human presence is more likely, the maximum EMF is recorded at 7.02 uT. This value is substantially below the ICNIRP 2010 reference level of 27 uT for General Public Exposure.

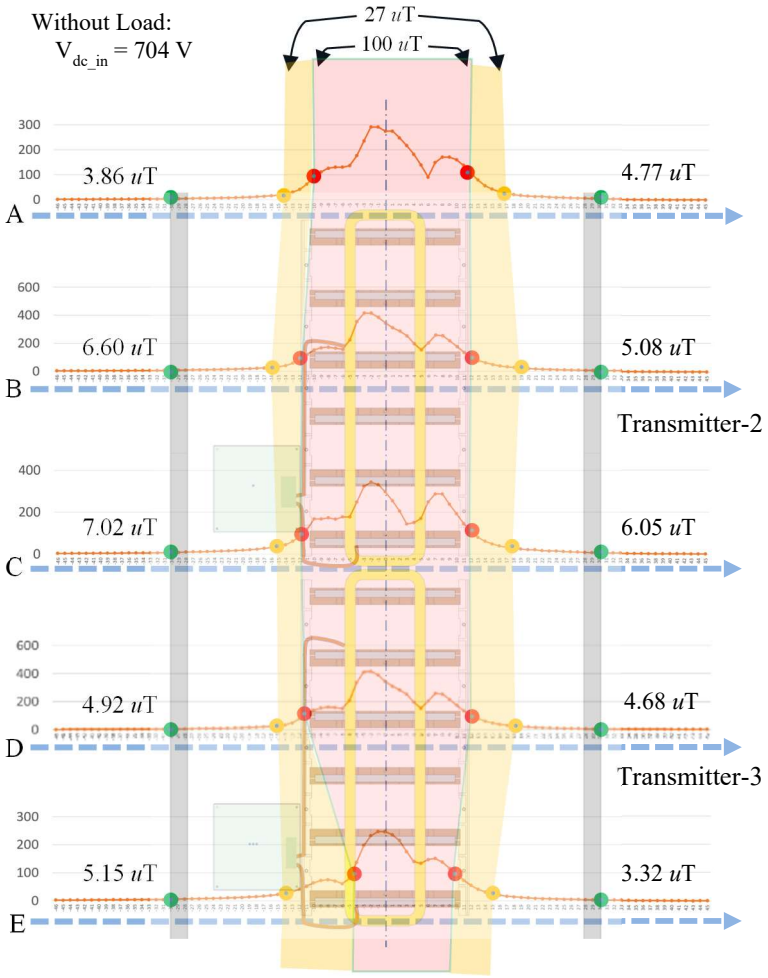

Figure 5-13: EMF measurements at different cross-sections of the transmitters

5.3.3 Dynamic EMF Measurements

For the dynamic charging measurement, the STSR setup was utilized. In this setup, the receiver is mounted on the movable platform and receives a charge as it passes over the transmitter. The EMF measurements were focused on the center of the movable platform, about 15 inches above the receiver coil, which is indicated as Position A in Figure 5-14.

As illustrated in Figure 5-14, during dynamic charging, there is a noticeable correlation between the receiver's proximity to the transmitter and the EMF values. Specifically, as the receiver gradually approaches the transmitter, the EMF value increases

correspondingly. The EMF reaches its peak at 38.709 *u*T when the receiver is directly aligned with the transmitter. Subsequently, as the receiver continues to move away, the EMF value diminishes gradually.

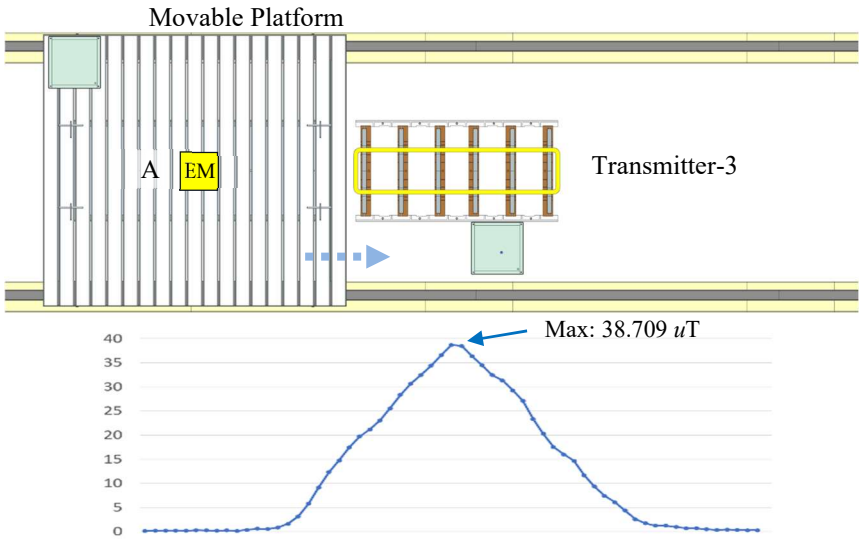

Figure 5-14: EMF measurements of dynamic charging with STSR

The maximum EMF value recorded on the trailer exceeds the ICNIRP 2010 standard limit of 27 *u*T set for General Public Exposure. Consequently, when implementing this system, it may be necessary to consider incorporating a shielding method to ensure compliance with these safety standards.

CHAPTER 6: FUTURE APPLICATION

6.0 Introduction

Wireless charging technology in railway systems is primarily in the research phase and has not yet reached widespread practical application. Consequently, this chapter concentrates on potential future application scenarios. The Belmont Trolley project will be used as a case study to discuss the specifics of project implementation. Additionally, a new concept involving wireless charging for power transport will be introduced.

6.1 Belmont Trolley Project

6.1.1 Project Description

Belmont City, located approximately ten miles west of Charlotte, NC, is home to a non-profit organization called “Belmont Trolley.” This entity is actively involved in restoring three historical trolleys, each boasting a rich legacy that dates back a century. The goal of the project is to reintroduce these trolleys along the city's old railway tracks, thereby reviving the trolley service. This initiative aims to rejuvenate the local community and boost tourism-related revenue for the city. Figure 6-1 showcases the three historical trolleys at Belmont Trolley.

In a collaborative effort, the University of North Carolina at Charlotte is lending its support to both Belmont City and Belmont Trolley. The university is contributing to the planning, design, and construction phases of the project. A key feature of this collaboration is the integration of wireless charging technology, which will not only enhance the technical aspects of the trolleys but also add to their appeal.

Figure 6-1: Three historical trolleys at Belmont Trolley

6.1.2 Technical Feasibility

The historical trolleys were originally designed to be powered by electric motors connected to an overhead power line. In this project, a new technical solution is adopted to circumvent the high costs and lengthy construction period associated with updating the infrastructure. The plan involves modifying a railway trailer to equip it with high-voltage batteries, an onboard charger, WPT receiver equipment, and other necessary devices. This trailer will supply power to the trolley and accompany it on the rails. At each station, WPT transmitter equipment will be installed between the tracks to wirelessly charge the high-voltage batteries while the trolley is parked.

According to the restoration plan, the trolley track spans 7,524 feet (1.425 miles) and includes five stops. The journey starts at Trolley Barn Station and ends at Belmont Abbey College Station, with the trolley scheduled to make 8 round trips each day. The trolleys will have a 30-minute rest period at the start and end stations, and a 3-minute stop at intermediate stations. The average speed will be 4.47 m/s, amounting to an approximate round trip running time of 36 minutes. Figure 6-2 illustrates the concept of a trolley station

equipped with a WPT system for the Belmont Trolley.

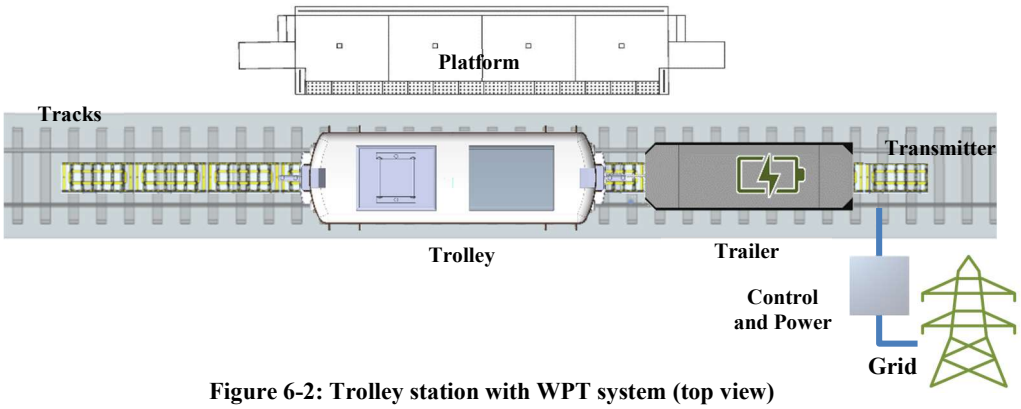

Figure 6-2: Trolley station with WPT system (top view)

The WPT system control and power module, located on the ground near the station, draws power from the grid and generates control signals and high-frequency AC for the system. This module activates the system only when a trolley is parked at the station.

The transmitters, installed between the tracks at the station, transmit power to the receiver mounted under the trailer. To minimize misalignment between the transmitter and receiver, multiple transmitters are used.

When the trolley is parked at a station, the control and power module powers on the system, enabling the transmitters to wirelessly transfer power to the receiver. The receiver then channels this power to the trailer, and the onboard charger replenishes the high-voltage (HV) battery. As the trolley departs, the control and power module deactivates the system, halting the charging process. To ensure passenger safety, only the transmitters located under the trailer are activated, while others remain off.

The entire wireless charging process is automated, offering technical advancement and convenience over traditional cable charging methods. This feature adds significant value to the Belmont Trolley project

6.1.3 Charging Analysis

The battery equipped in the trolley has a capacity of 40 kWh. Based on previous research, the total energy requirement for one round trip is estimated to be 13.94 kWh. Without any mid-service charging, the trolley would only be able to complete three round trips, which falls short of the required eight trips. To address this limitation, WPT technology is incorporated into the project to enable battery charging either when the trolley is stationary or in motion, as needed.

Two charging device sets will be installed at both the start and end stations of the WPT system. Each charging station will be equipped with two receivers, providing a charging power of 12 kW. During the 30-minute rest period at each station, the battery is expected to receive 6 kWh of charge, amounting to a total of 12 kWh for one round trip.

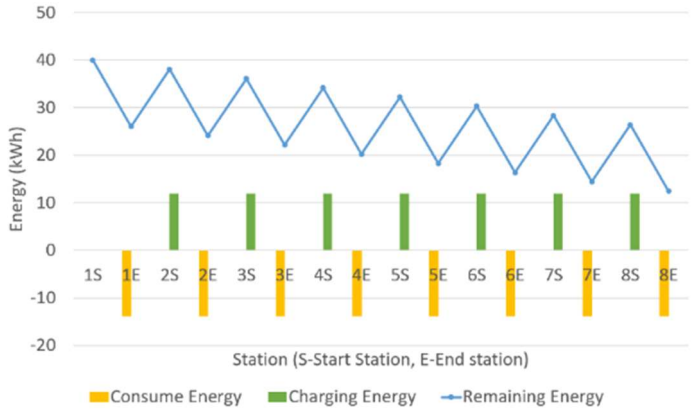

Figure 6-3: Battery remaining power for eight round trips

Figure 6-3 illustrates the battery's remaining power curve over the course of eight round trips in a single day. At the start of the first round trip (1S), the battery's energy level is at 40 kWh. After consuming 13.94 kWh, the energy level drops to 26.06 kWh at the end of the first round trip (1E). Before the start of the second round trip (2S), the battery receives a 12 kWh charge, reducing the energy consumption to 1.94 kWh per trip. Following each

charging session, the trolley embarks on the next trip. After completing eight round trips (8E), the battery has 12.48 kWh of energy remaining.

Should there be a need for additional trips, the energy requirement will increase correspondingly. Two solutions can be employed to meet this higher energy demand: The first option is to extend the parking time at each station; the second is to install additional transmitters between stations to facilitate dynamic charging.

6.1.4 Cost Analysis

The Belmont Trolley project encompasses a variety of tasks across civil, mechanical, and electrical engineering disciplines. These tasks include building new stations and modifying the trailer for the trolley system. According to estimates from previous research, the cost of constructing five stations and modifying the vehicles is outlined in Table 6-1. The total estimated cost for these components of the project amounts to $197,248.00.

Table 6-1: Cost of stations and trailer

Item	Cost
Trolley Barn Station	$35,783.00
East Woodrow Avenue Station	$64,387.00
Sacred Heart Campus Station	$23,721.00
Main street Bi Lo Station	$25,560.00
Belmont College Station	$26,860.00
Trailer Modification	$20,937.00
Total	$197,248.00

For the WPT system, the costs are listed in Table 6-2 and Table 6-3.

Table 6-2: Cost of the WPT per station

Item	Cost	Quantity	Subtotal
Control and Power Module	24,000.00	1	24,000.00
Transmitter	5,000.00	3	15,000.00
Total	--	--	39,000.00

Table 6-3: Cost of the WPT for a trailer

Item	Cost	Quantity	Subtotal
Receiver	10,000.00	2	20,000.00
Total	--	--	20,000.00

In this project, the installation of WPT devices is required at two stations and on one trailer. Consequently, the total cost for incorporating these WPT devices into the project amounts to $295,248.00. In comparison, other solutions, such as overhead power lines, can incur significantly higher costs. The construction expenses for rail infrastructure with overhead power lines can range from $2 million per mile in flat rural areas to as much as $300 million per mile in urban settings, as indicated by references [21, 59]. Even opting for the most economical approach, the cost for implementing overhead power lines along the 1.425 miles of railway in Belmont would amount to approximately $2.85 million. Therefore, by adopting WPT technology for the railway transformation in Belmont, investment savings of up to 89.64% could be realized.

6.2 Energy Transport

Potential future applications of this system also encompass “Energy Transport,” where electricity from areas with abundant energy but low demand is transported via train to regions with high demand but low energy availability. For instance, in the Midwest of the United States, large desert areas are rich in renewable energy sources, such as solar and wind power. However, due to the lack of grid infrastructure in these sparsely populated areas, the potential for solar farms or wind power plants is unrealized because the generated power cannot be distributed.

In such scenarios, locomotives could serve as mobile electricity containers, facilitating the transit of energy between different areas. Figure 6-4 illustrates the concept

of "Energy Transport." In location A, energy is harvested from solar farms and wind plants but remains grid-isolated. Here, the energy is stored in an energy storage unit. As a locomotive passes through, it can charge its battery bank via the WPT system. In location B, where utility services exist, the locomotive can discharge power into the grid using WPT. Additionally, the locomotive can also be recharged at location B if necessary.

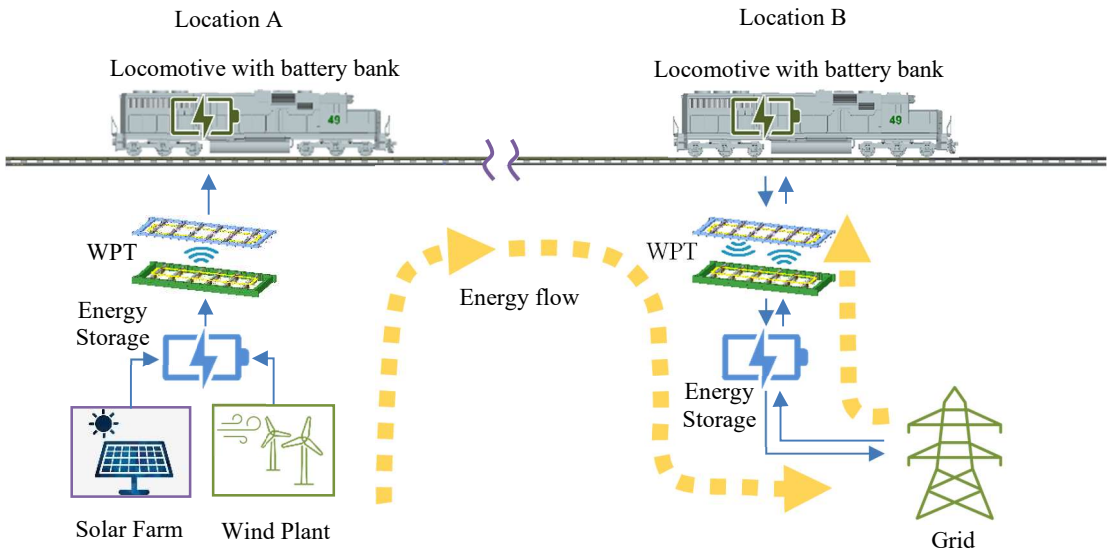

Figure 6-4: Concept of energy transport

Some requirements for this concept differ from those of standard WPT applications for locomotives. Firstly, the locomotive functions as a movable battery, necessitating a significantly larger battery bank to store more energy. Secondly, the amount of energy transmitted per unit of time could be considerably greater than that in ordinary applications. This increase in energy transmission demands a higher power circuit, making it essential to optimize the design to meet specific voltage, current, and efficiency requirements. Thirdly, as the locomotive needs to transfer energy back to the grid, the WPT system must be capable of bidirectional operation. Beyond these technical considerations, economic aspects are equally important and warrant further study and prioritization.

CHAPTER 7: CONCLUSIONS AND FUTURE WORKS

7.1 Conclusions

This thesis explores wireless power transfer (WPT) technologies, focusing on their application in railway electrification. The study has successfully developed and tested a novel 6 kW WPT system for railway vehicles, employing a parallel synchronous multiple LCL-S compensation topology. This system has demonstrated significant potential in improving the efficiency and reliability of power transfer for railway electrification.

The prototype' achieved a remarkable DC-to-DC efficiency of 94.73% in static testing with an input of 727.05 V DC at an output of 3.0 kW. These results highlight the system's capability to deliver high power efficiency. The dynamic tests further validated the system's performance under motion, showing that the output remained stable and the efficiency consistently high. This is crucial for applying WPT in dynamic railway environments where stability and efficiency are critical.

The study gave special attention to developing an optimized protocol for the interaction between multiple transmitters and a single receiver. This protocol is a pivotal system component, ensuring synchronized power delivery and maintaining efficiency under various operational conditions.

Electromagnetic Field (EMF) testing was conducted to ensure the safety and compliance of the WPT system with health standards. The results from these tests were reassuring, confirming the system's suitability for practical application while adhering to safety regulations.

The thesis also explored various application scenarios for the WPT system,

highlighting its versatility in different railway contexts. This includes retrofitting existing railway systems and integration into newly constructed networks. The study underscores the potential of WPT technology in revolutionizing railway electrification, offering a sustainable and efficient solution to modern transportation challenges.

In conclusion, this research explores the future development of WPT systems in railway applications. It offers a comprehensive solution that combines technical innovation, operational efficiency, and safety considerations, contributing to railway electrification.

7.2 Future Work

(1) Enhancing system capacity and efficiency

Future work should focus on increasing the power capacity of the WPT system beyond the current 6 kW level. This involves optimizing the system design to handle higher power levels while maintaining or improving efficiency. Research into advanced materials and technologies could yield significant improvements in this regard.

(2) Expanding the scope of dynamic testing

While the current study has provided promising results in dynamic testing, further research under a broader range of operational conditions is necessary. This includes testing the WPT system on railway tracks under various speeds, loads, and environmental conditions to validate its practicality and robustness in real-world scenarios.

(3) Automated and smart control systems

Developing intelligent control systems for managing the WPT system efficiently is another potential area of research. This includes using machine learning algorithms and IoT technologies for real-time monitoring, predictive maintenance, and adaptive power management.

(4) Advanced EMF safety standards and regulations

Continuing research on EMF emissions and compliance with safety standards is vital. Future work should aim at developing more stringent safety protocols and guidelines, ensuring the WPT system's adherence to evolving health and safety regulations.

(5) Application scenarios

Investigating the application of WPT technology in other types of railways, such as high-speed trains, Maglev, and urban transit systems, would be beneficial. Assessing the scalability and adaptability of the system to different railway architectures and operational demands is crucial for broader applicability.

REFERENCES

1. AAR. *U.S. Freight Railroad Industry Snapshot*. 2023; Available from: https://www.aar.org/data-center/railroads-states/.
2. bts.gov. *Class I Railroad Locomotive Fleet by Year Built*. 2023; Available from: https://data.bts.gov/stories/s/Freight-Transportation-System-Condition-Performanc/vvk5-xjjp/.
3. Hu, P.S., Rolf R.; Robinson, Ramond; Nguyen, Long; Moore, William H.; Baunee, Aaron; Culotta, Kalle; Hocevar, Hannah; Kimmel, Sari; Stacey, Mikki; Wingfield, Alpha;, *Transportation Statistics Annual Report 2022*. 2022.
4. Nunno, R. *Electrification of U.S. Railways: Pie in the Sky, or Realistic Goal?* 2018; Available from: https://www.eesi.org/articles/view/electrification-of-u.s.-railways-pie-in-the-sky-or-realistic-goal.
5. Gordon, W. *Electrified rail is the future. Is Virginia all aboard?* 2023 JANUARY 9, 2023; Available from: https://www.virginiamercury.com/2023/01/09/electrified-rail-is-the-future-is-virginia-all-aboard/.
6. AAR, *Oppose Rail Electrification*. 2020.
7. RailTEC, *Transitioning to a zero or near-zero emission line-haul freight rail system in California: Operational and economic considerations*. 2016, Report Prepared to State of California Air Resources Board United States.
8. Popovich, N.D., et al., *Economic, environmental and grid-resilience benefits of converting diesel trains to battery-electric.* Nature Energy, 2021. **6**(11): p. 1017-1025.
9. Xu, X., *Wireless Power Transfer for Railway Applications*. 2022, The University of North Carolina at Charlotte.
10. Tesla, N., *Apparatus for transmitting electrical energy*. 1914, Google Patents.
11. Weiss, H., T. Winkler, and H. Ziegerhofer. *Large lithium-ion battery-powered electric vehicles—From idea to reality*. in *2018 ELEKTRO*. 2018. IEEE.
12. Ahmad, S., et al., *Analysis of positioning of wayside charging stations for hybrid locomotive consists in heavy haul train operations.* Railway Engineering Science, 2021. **29**: p. 285-298.
13. Iden, M.E. *Battery Electric Locomotives & Battery Tenders: Operational & Infrastructure Challenges to Widespread Adoption*. in *ASME/IEEE Joint Rail Conference*. 2021. American Society of Mechanical Engineers.
14. Xu, X., et al. *Design Considerations of An Inductive Power Transfer System for Rail Application*. in *2021 IEEE Transportation Electrification Conference & Expo (ITEC)*. 2021. IEEE.
15. Zhang, Z., et al., *Wireless power transfer—An overview.* IEEE transactions on industrial electronics, 2018. **66**(2): p. 1044-1058.
16. Mohamed, A.A., A. Meintz, and L. Zhu, *System design and optimization of in-route wireless charging infrastructure for shared automated electric vehicles.* IEEE Access, 2019. **7**: p. 79968-79979.
17. Mohamed, A., A. Meintz, and K. Walkowicz, *Planning of In-motion Electric Vehicle Charging on Freeways.* Planning, 2020.
18. Nguyen, D.M., M.A. Kishk, and M.-S. Alouini, *Toward sustainable transportation: Accelerating vehicle electrification with dynamic charging deployment.* IEEE Transactions on Vehicular Technology, 2022. **71**(9): p. 9283-9296.
19. Rozman, M., et al., *Smart wireless power transmission system for autonomous EV charging.* IEEE Access, 2019. **7**: p. 112240-112248.
20. Mude, K. and K. Aditya, *Comprehensive review and analysis of two-element resonant compensation topologies for wireless inductive power transfer systems.* Chinese Journal of Electrical Engineering, 2019. **5**(2): p. 14-31.
21. Abel, E. and S. Third, *Contactless power transfer--An exercise in topology.* IEEE Transactions on Magnetics, 1984. **20**(5): p. 1813-1815.
22. Wang, C.-S., G.A. Covic, and O.H. Stielau, *Power transfer capability and bifurcation phenomena of loosely coupled inductive power transfer systems.* IEEE transactions on industrial electronics, 2004. **51**(1): p. 148-157.

23. Elliott, G.A., et al., *A new concept: Asymmetrical pick-ups for inductively coupled power transfer monorail systems.* IEEE Transactions on Magnetics, 2006. **42**(10): p. 3389-3391.
24. Kacprzak, D., G. Covic, and J.T. Boys. *An improved magnetic design for inductively coupled power transfer system pickups*. in *2005 International Power Engineering Conference*. 2005. IEEE.
25. Jiang, Y., et al., *Designing an M-shape magnetic coupler for the wireless charging system in railway applications.* IEEE Transactions on Power Electronics, 2021. **37**(1): p. 1059-1073.
26. Lee, J.-Y., H.-Y. Shen, and K.-C. Chan, *Design and implementation of removable and closed-shape dual-ring pickup for contactless linear inductive power track system.* IEEE Transactions on Industry Applications, 2014. **50**(6): p. 4036-4046.
27. Moriki, K., et al. *Efficiency study of coaxial contactless power transmission for electric railway*. in *2015 17th European Conference on Power Electronics and Applications (EPE'15 ECCE-Europe)*. 2015. IEEE.
28. Xu, L., et al. *A novel contactless transformer with trapezoidal windings cross section in IPT system for movable vehicle*. in *2016 19th International Conference on Electrical Machines and Systems (ICEMS)*. 2016. IEEE.
29. Shi, L., et al., *Advances in inductively coupled power transfer technology for rail transit.* CES Transactions on Electrical Machines and Systems, 2017. **1**(4): p. 383-396.
30. Ukita, K., et al. *Evaluation of a non-contact power supply system with a figure-of-eight coil for railway vehicles*. in *2015 IEEE PELS Workshop on Emerging Technologies: Wireless Power (2015 WoW)*. 2015. IEEE.
31. Park, C.-B., *A study on the high-efficiency coreless-typed wireless power transfer system for railway transit.* Journal of Electrical Engineering & Technology, 2016. **11**(5): p. 1305-1310.
32. Wang, L., et al. *An Inductive Power Transfer System Design for Rail Applications*. in *2018 IEEE Transportation Electrification Conference and Expo (ITEC)*. 2018. IEEE.
33. Huh, J., et al. *High performance inductive power transfer system with narrow rail width for on-line electric vehicles*. in *2010 IEEE Energy Conversion Congress and Exposition*. 2010. IEEE.
34. Huh, J., et al., *Narrow-width inductive power transfer system for online electrical vehicles.* IEEE Transactions on Power Electronics, 2011. **26**(12): p. 3666-3679.
35. Shin, J., et al. *Optimal current control of a wireless power transfer system for high power efficiency*. in *2012 Electrical Systems for Aircraft, Railway and Ship Propulsion*. 2012. IEEE.
36. Lee, C.H., et al. *Design and introduction of high power transfer system for electrical vehicles*. in *2013 IEEE International Conference on Intelligent Rail Transportation Proceedings*. 2013. IEEE.
37. Hao, H., G.A. Covic, and J.T. Boys, *A parallel topology for inductive power transfer power supplies.* IEEE Transactions on Power Electronics, 2013. **29**(3): p. 1140-1151.
38. Shin, J., et al., *Design and implementation of shaped magnetic-resonance-based wireless power transfer system for roadway-powered moving electric vehicles.* IEEE Transactions on Industrial electronics, 2013. **61**(3): p. 1179-1192.
39. Kim, J.H., et al., *Development of 1-MW inductive power transfer system for a high-speed train.* IEEE Transactions on Industrial Electronics, 2015. **62**(10): p. 6242-6250.
40. Choi, S.Y., et al., *Ultraslim S-type power supply rails for roadway-powered electric vehicles.* IEEE Transactions on Power Electronics, 2015. **30**(11): p. 6456-6468.
41. Li, Y., et al., *Efficiency analysis and optimization control for input-parallel output-series wireless power transfer systems.* IEEE Transactions on Power Electronics, 2019. **35**(1): p. 1074-1085.
42. Anyapo, C. and P. Intani. *Development of Long Rail Dynamic Wireless Power Transfer for High-Speed Train*. in *2019 16th International Conference on Electrical Engineering/Electronics, Computer, Telecommunications and Information Technology (ECTI-CON)*. 2019. IEEE.
43. Luo, B., et al., *Misalignment tolerance wireless power transfer system combining inductive and capacitive coupling.* IET Electric Power Applications, 2020. **14**(10): p. 1925-1932.
44. Geng, Y., Z. Yang, and F. Lin, *Design and control for catenary charged light rail vehicle based on wireless power transfer and hybrid energy storage system.* IEEE Transactions on Power Electronics, 2020. **35**(8): p. 7894-7903.
45. Deng, J., et al., *The design and coupler optimization of a single-transmitter coupled multireceiver inductive power transfer system for maglev trains.* IEEE Transactions on Transportation Electrification, 2021. **7**(4): p. 3173-3184.

46. Lee, C.H., et al. *Wireless power transfer system for an autonomous electric vehicle*. in *2020 IEEE Wireless Power Transfer Conference (WPTC)*. 2020. IEEE.
47. Song, B., et al., *A narrow-rail three-phase magnetic coupler with uniform output power for EV dynamic wireless charging.* IEEE Transactions on Industrial Electronics, 2020. **68**(8): p. 6456-6469.
48. Rea, E.A.S., *Scaled Down Dynamic Wireless Power Transfer for Railroad Applications*. 2020, The University of North Carolina at Charlotte.
49. Hernando, F.G., et al. *Dynamic ipt system with lumped coils for railway application*. in *2017 19th European Conference on Power Electronics and Applications (EPE'17 ECCE Europe)*. 2017. IEEE.
50. Dwinanto, A.Y. and Y.-C. Liu. *Design and analysis for dynamic wireless power transfer based on circular railway with continuous dynamic loads*. in *2021 IEEE/ASME International Conference on Advanced Intelligent Mechatronics (AIM)*. 2021. IEEE.
51. Wang, Z., et al., *A novel magnetic coupling mechanism for dynamic wireless charging system for electric vehicles.* IEEE Transactions on Vehicular Technology, 2017. **67**(1): p. 124-133.
52. Lin, K., et al. *Passive Shielding Design of an Inductive Power Transfer System for Railway Applications*. in *2022 IEEE Transportation Electrification Conference & Expo (ITEC)*. 2022. IEEE.
53. Lee, G., et al., *Electromagnetic field tests of a 1-MW wireless power transfer system for light rail transit.* Energies, 2021. **14**(4): p. 1171.
54. Ryu, H.-G. and D. Har. *Wireless power transfer for high-precision position detection of railroad vehicles*. in *2015 IEEE Power, Communication and Information Technology Conference (PCITC)*. 2015. IEEE.
55. Hwang, K., et al., *Pickup coil counter for detecting the presence of trains operated by wireless power transfer.* IEEE Sensors Journal, 2017. **17**(22): p. 7526-7532.
56. Kongwarakom, W., T. Ratniyomchai, and T. Kulworawanichpong. *Analysis and Design of Wireless Charging Lane for Light Rail Transit*. in *2020 International Conference on Power, Energy and Innovations (ICPEI)*. 2020. IEEE.
57. ICNIRP, *Guidelines for limiting exposure to time-varying electric, magnetic, and electromagnetic fields (up to 300 GHz).* Health physics, 1998. **74**(4): p. 494-522.
58. ICNIRP, *Guidelines for limiting exposure to time-varying electric and magnetic fields (1 Hz to 100 kHz).* Health physics, 2010. **99**(6): p. 818-836.
59. National Academies of Sciences, E. and Medicine, *Alternative Funding and Financing Mechanisms for Passenger and Freight Rail Projects*. 2015.

APPENDIX A: Photos of the WPT System

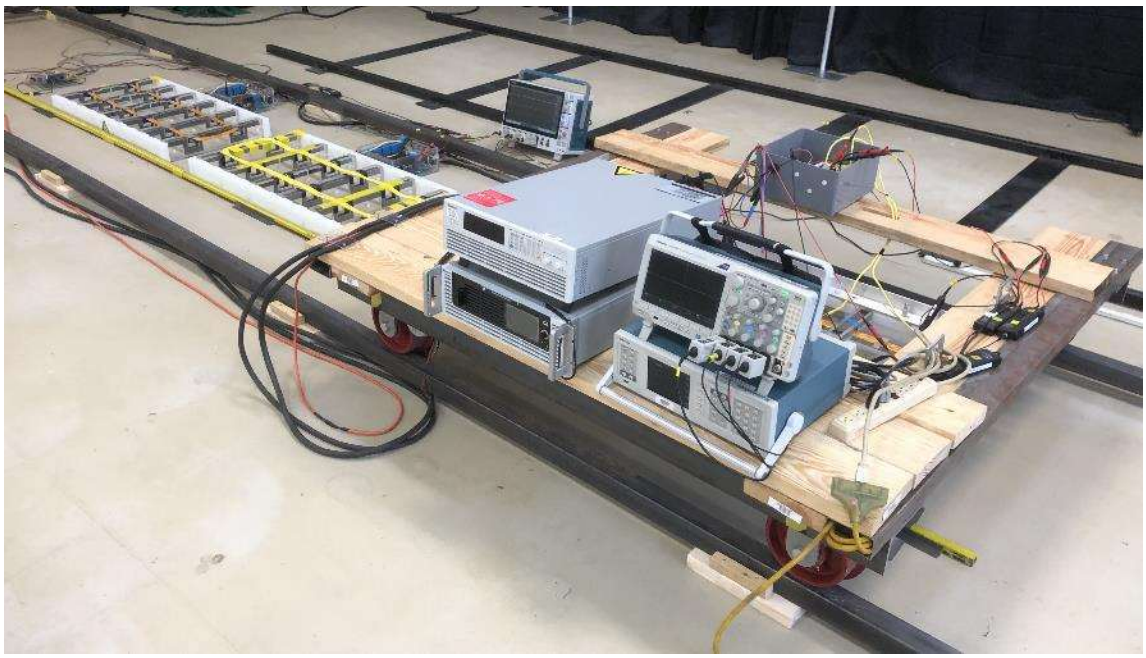

Figure A-1: Overlook of the WPT prototype-1.

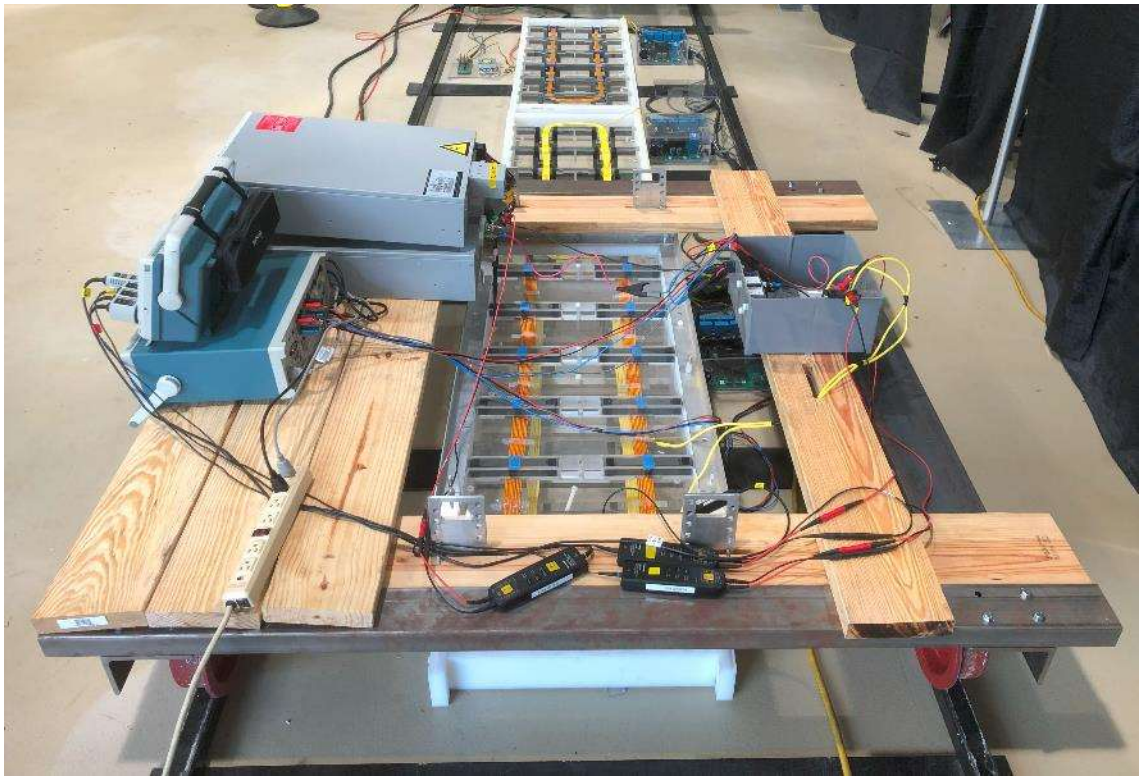

Figure A-2: Overlook of the WPT prototype-2

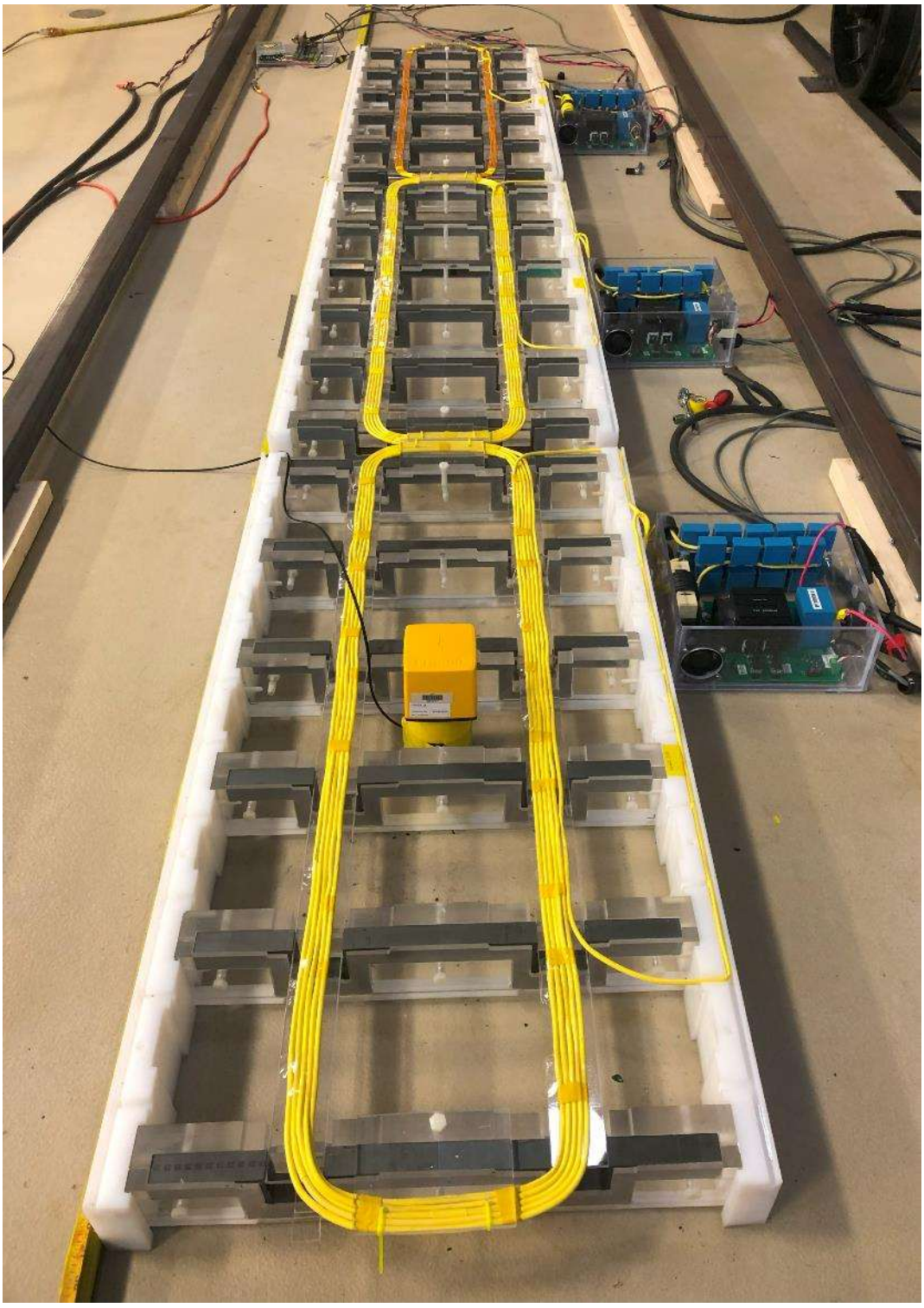

Figure A-3: Overlook of three transmitters

Figure A-4: Transmitter-2 and inverter

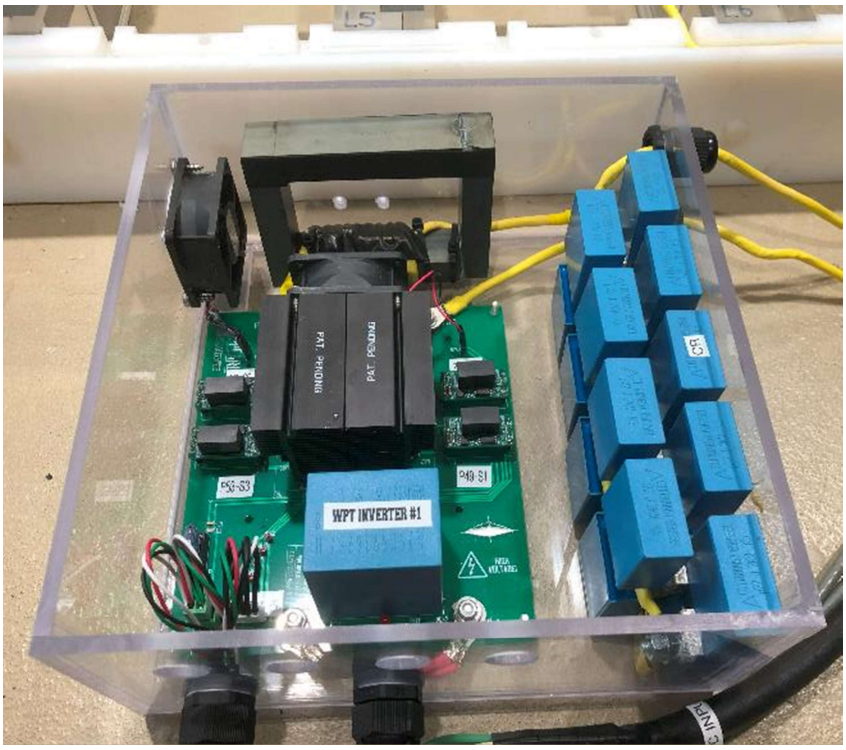

Figure A-5: Inverter-1.

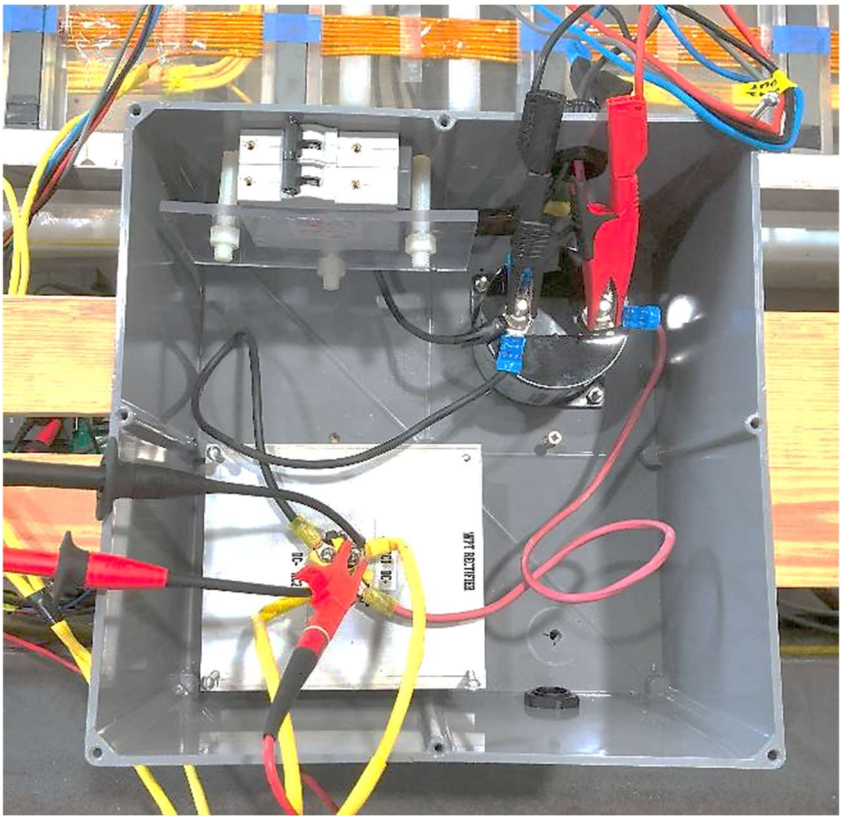

Figure A-6: Rectifier of receiver

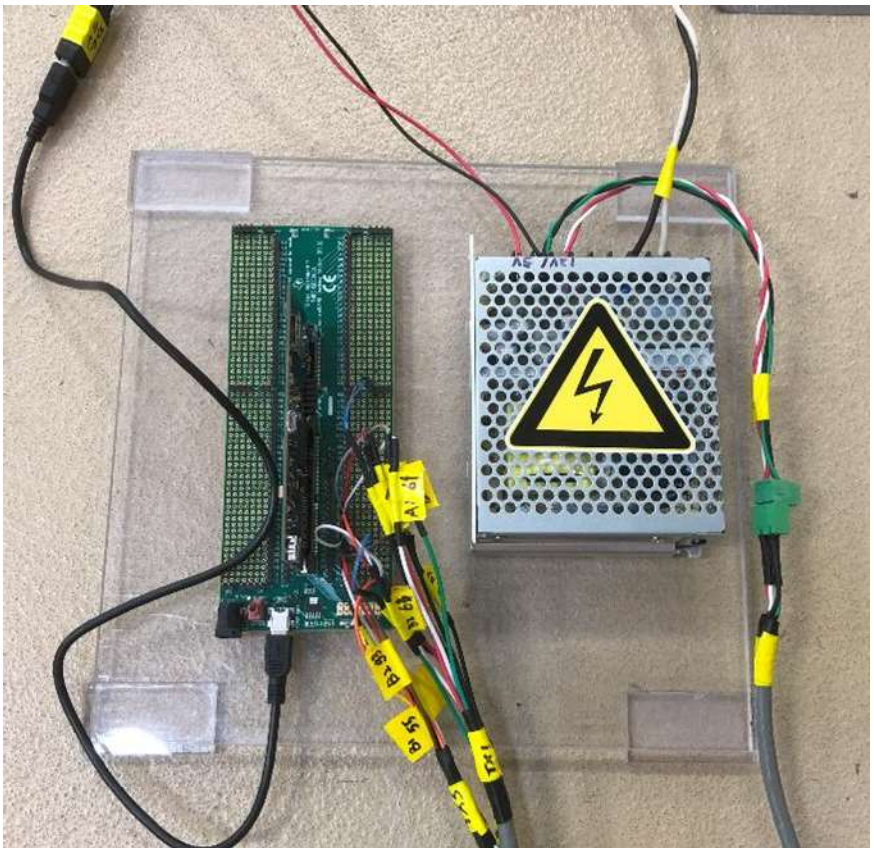

Figure A-7: Frequency generator and additional power supply.

Figure A-8: Transmitter (lower) and receiver (upper) under movable platform

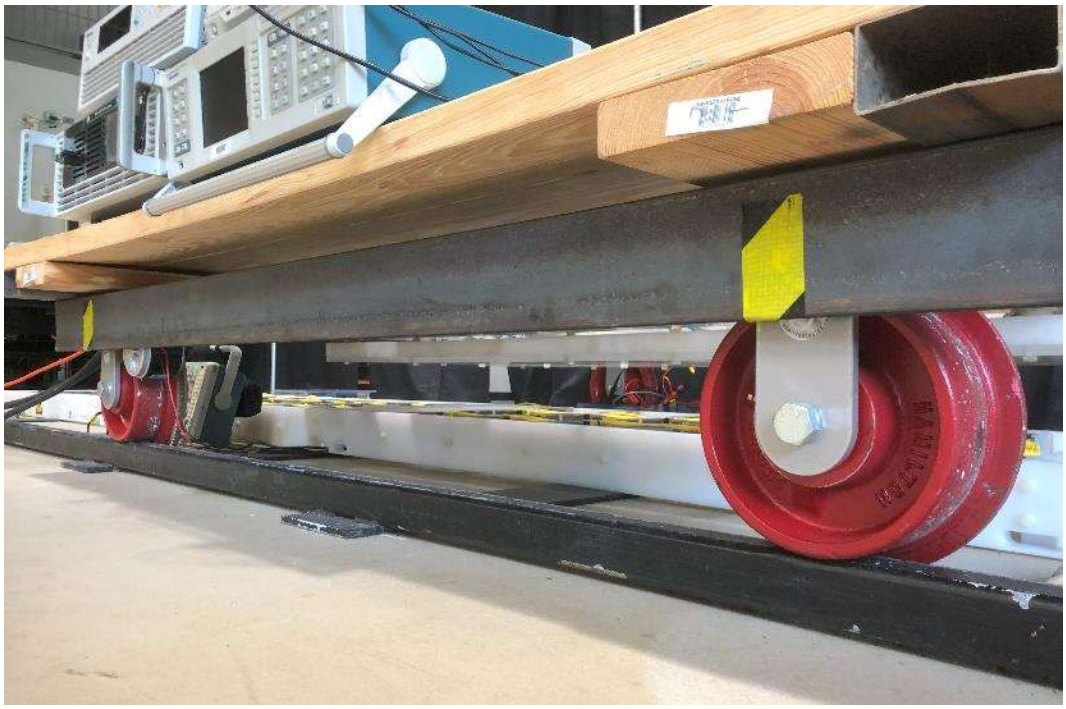

Figure A-9: Wheels and frame of movable platform